Identification of mechanisms of magnetic transitions using an efficient method for converging on first-order saddle points

Hendrik Schrautzer [1,*] Moritz Sallermann [1,2,3,*] Pavel F. Bessarab [1,4,†] and Hannes Jónsson [1]

[1] *Science Institute and Faculty of Physical Sciences, University of Iceland, VR-III, 107 Reykjavík, Iceland*

[2] *Peter Grünberg Institut and Institute for Advanced Simulation, Forschungszentrum Jülich and JARA, 52425 Jülich, Germany*

[3] *Department of Physics, RWTH Aachen University, 52056 Aachen, Germany*

[4] *Department of Physics and Electrical Engineering, Linnaeus University, SE-39231 Kalmar, Sweden*

(Received 23 December 2024; revised 1 July 2025; accepted 22 August 2025; published 24 September 2025)

An efficient and scalable implementation of a method for locating first-order saddle points on the energy surface of a magnetic system is presented, along with several applications in which the mechanisms of various magnetic transitions are identified. The starting point for the iterative search algorithm can be anywhere, even close to a local energy minimum representing an initial state of the system, and the final state need not be specified. Convergence on a saddle point is obtained by inverting the component of the gradient along the minimum mode, thereby effectively transforming the neighborhood of the saddle point to that of a local minimum. The method requires only the lowest two eigenvalues and corresponding eigenvectors of the Hessian of the system's energy and they are found using a quasi-Newton limited-memory Broyden-Fletcher-Goldfarb-Shanno solver for the minimization of the Rayleigh quotient without explicit evaluation of the Hessian. The method is applicable to large systems, as it does not introduce additional scaling overhead to the computational complexity determined by the interactions present in the system. Applications are presented to transitions in systems that reveal significant complexity of coexisting magnetic states, such as skyrmions, skyrmion bags, skyrmion tubes, chiral bobbers, and globules. The identification of new metastable three-dimensional (3D) textures, such as magnetic bobbers with extended equilibrium distance between the base and the terminating Bloch point, and magnetic globules appearing as isolated states in 3D due to magnetostatic interactions, demonstrates the usefulness of the method for the characterization of complex energy surfaces of magnetic systems. When combined with rate theory within the harmonic approximation, the method can be used for simulations of the long timescale dynamics of complex magnetic systems characterized by multiple metastable states.

DOI: 10.1103/z673-hhnp

I. INTRODUCTION

The task of identifying the mechanism of possible transitions and estimating the corresponding rate within harmonic transition state theory (HTST) [1,2] or Kramers/Langer theory [3,4] involves finding low-lying first-order saddle points (SPs) on the energy surface that specifies how the energy of the system varies as a function of the various degrees of freedom. A first-order SP is an extremal point, i.e., of zero gradient, where one and only one eigenvalue of the Hessian of the energy of the system is negative. It is challenging to locate an SP because of the need to maximize the energy with respect to one degree of freedom while it is minimized with respect to all others, as it is not known *a priori* which degree of freedom to treat separately [5]. If, in addition to the initial state, the final state of the transition is known, the minimum energy path (MEP) between the two corresponding minima on the energy surface can be found [6,7], and the relevant SP located as the point of highest energy along the path. However, various applications, such as a simulation of long timescale dynamics using the adaptive kinetic Monte Carlo algorithm [8,9], necessitate the identification of likely transitions without any prior assumptions about final states. This is a more challenging task than the calculation of a minimum energy path for given initial and final states and can lead to the discovery of transition mechanisms into unexpected final states. SP searches can also be used as the basis for global optimization of an objective function in a broader context [10], as well as for path optimization [11], e.g., in calculations of tunneling within instanton theory [12,13] and radio wave propagation [14]. An efficient algorithm for locating SPs can, therefore, have wide applicability.

The development of SP search methods that do not require knowledge of the final state has, primarily, been in the context of atomic rearrangements, such as diffusion and chemical reactions [15]. There, an SP search typically starts near the local energy minimum representing an initial state of the system and is carried out in two stages. First, the system is

*These authors contributed equally to this work.

†Contact author: pavel.bessarab@lnu.se

driven out of the convex region where all eigenvalues of the Hessian of the energy are positive. Second, after the lowest eigenvalue turns negative, an algorithm for converging on the nearest SP is used. The first phase can be done in several different ways. In eigenvector following methods that are often used in studies of atomic rearrangements in small systems, the Hessian is evaluated and the eigenvalue problem solved to determine the eigenvectors. Various search paths are then generated starting from the minimum by following each one of the eigenvectors uphill until the convex region has been exited [15]. A more efficient approach, especially for large systems, is to generate several starting points by displacing the system in some random way from the minimum and then moving uphill along the eigenvector corresponding to the lowest eigenvalue, the so-called minimum mode, until the lowest eigenvalue turns negative [16]. Alternatively, the system can be pushed further along the direction defined by the difference between the starting configuration and the minimum while the energy is minimized in orthogonal directions [17]. Several ways have been introduced for generating the starting configurations, for example, Gaussian distributed displacements of the atoms from the minimum in some subregion of the system [18] or evenly distributed points on the surface of a hypersphere with radius pushed out to the edge of the convex region [19].

In the second stage, after escaping the convex region, the force acting on the atoms, i.e., the negative gradient of the energy with respect to atom coordinates, is modified by inverting the component along the minimum mode and the atoms displaced so as to zero this modified force. This ensures energy maximization along only the minimum mode and minimization along all other directions. Such a path eventually convergences on an SP. This technique is referred to as minimum mode following (MMF) method. Thus, the search path is guided by the uphill direction of the minimum mode, while the energy is minimized with respect to all perpendicular directions. The minimum mode can be found by using, for example, the dimer [16], Lanczos [17,20], or Davidson [19,21] methods without even evaluating the Hessian matrix.

Since the starting point of an SP search can be anywhere on the energy surface, MMF can also be used to converge on an SP starting from an approximate estimate, coming, for example, from a partially converged nudged elastic band calculation [6]. Such a combination of an MEP finding method that is only partially converged followed by an SP search method starting from the point of highest energy along the obtained path, provides the most efficient way of converging on an SP corresponding to a transition to a given final state [12].

The rate of magnetic transitions, i.e., transitions where magnetic moments rotate, can in a similar manner be estimated by identifying SPs on the energy surface of a magnetic system [22–24]. When both initial and final states are specified, the minimum energy path can be found using the geodesic nudged elastic band method (GNEB) or the climbing image version CI-GNEB, where the highest-energy image is pushed up to the maximum along the path [7]. This method has been used, for example, to study the collapse of localized magnetic structures such as skyrmions [25–32] as well as textures beyond skyrmions [33–36] including three-dimensional (3D) states such as hopfions or skyrmion tubes [37–42].

When investigating transitions between topological magnetic textures using the GNEB method, generating appropriate initial paths can be challenging and often requires intuition. For example, a linear interpolation between the initial and final states is often not sufficient for the identification of transitions involving translations of a magnetic texture.

Similarly to atomic rearrangements, the search for SPs without specifying a final state or generating an initial path can be carried out for magnetic transitions. There, however, the curvature of the configuration space poses additional challenges as compared to the atomic rearrangements. The convergence on an SP involves rotating the magnetic moments using the force modified by an inversion along the minimum mode and projected onto the local tangent space of the current configuration. We refer to this as the geodesic minimum mode following (GMMF) method.

Analogous to the MMF method for atomic rearrangements, the GMMF method can be used to identify possible magnetic transitions from a given initial state without specifying a final state, thereby possibly discovering new and unexpected mechanisms and final states. Also, analogous to the atomic rearrangements, GMMF can be used in combination with a GNEB calculation that is not carried to completion, so as to converge on an SP corresponding to a transition to a known final state. The method can, furthermore, be generalized to find higher-order saddle points, and this has been shown to be an efficient way to calculate excited electronic states [43].

A straightforward implementation of the GMMF method would involve the evaluation of the Hessian and calculation of at least the lowest eigenvalue and corresponding eigenvector, as was done by Müller *et al.* [44]. However, the computational effort then increases rapidly with system size. The number of magnetic moments in relevant model systems can be large, often on the order of 10^5 to 10^7. Henceforth, even the mere evaluation of the full Hessian can require substantial effort. In particular, the explicit inclusion of long-range magnetostatic effects, as is frequently necessary in large three-dimensional systems, may not be feasible with such an approach. The reason is that the Hessian matrix then becomes dense and storing it can exceed the working memory capacity of a typical compute node, even for systems of moderate size. In addition, models that go beyond a simple Heisenberg approach, such as the noncollinear extension of the Alexander-Anderson model [45,46] and density functional theory calculations, make the computation of second-order derivatives a significant task.

After the introduction of the GMMF method by Müller *et al.* [44], it has been successfully used to identify mechanisms of magnetic transitions in several systems including the duplication of magnetic skyrmions [44], transformation of defects in skyrmion lattices [47], annihilation of three-dimensional hopfions [41], and transitions in a two-dimensional dipolar spin glass [47]. However, previous implementations of GMMF have been less than optimal in several respects, in that the full Hessian is explicitly evaluated and this limits the applicability of the method to rather small systems. Since the GMMF method strictly requires only the eigenvector corresponding to the lowest eigenvalue of the Hessian, the evaluation of the full Hessian is, in fact, not

needed. A more efficient implementation of GMMF is, therefore, possible and is described in detail in this article.

We report, in particular, an efficient way of computing the modified force in the GMMF method, using an iterative approach that does not require the evaluation of the Hessian. It is, thereby, applicable to large systems and more complex Hamiltonians than the Heisenberg form. Knowledge of the second lowest eigenvalue can also be useful to guide GMMF calculations, especially at mode crossings, as will be demonstrated below, and the method presented here is noteworthy in that the lowest two eigenvalues and corresponding eigenvectors are found simultaneously, using the generalized Rayleigh quotient and an L-BFGS optimizer on the Grassmann manifold.

The article is organized as follows. The method is described in Sec. II. This is followed by Sec. III, where the application systems are described. Results of several GMMF calculations are presented Sec. IV featuring various magnetic structures in two- and three-dimensional systems and the performance is compared to that of a partial eigenvalue calculation with the Intel Math Kernel Library [48]. The final section summarizes the main findings and discusses their implications. Six Appendices provide additional details: (A) description of the four-spin system used to illustrate mode crossings; (B) pseudocode for the Rayleigh quotient optimization; (C) full Hessian expressions for reference; (D) summary of numerical parameters used in the calculations; (E) results for a 3D system without magnetostatics; and (F) analysis of the method's scaling behavior.

II. METHOD

One important aspect of the GMMF method is the correct consideration of the configuration space $\mathcal{R}$ of magnetic systems which is a Riemannian manifold. Typically, the magnitude of the magnetic vectors is either assumed to be independent of orientation or treated as a fast variable within the adiabatic approximation. In the latter case, the magnitude is calculated for fixed orientations of the magnetic moments, which are considered to be slow variables [49]. In either case, the configuration space of a system with N magnetic moments is a direct product of two-dimensional spheres S_2 associated with each magnetic moment vector:

$$\mathcal{R} = \bigotimes_N S_2 \subset \mathbb{R}^{3N}, \tag{1}$$

giving rise to $2N$ degrees of freedom. Displacements in the configuration space correspond to rotations of the magnetic moments. It is computationally advantageous to work in the embedding space $\mathbb{R}^{3N}$ and to eliminate the N superfluous degrees of freedom by applying the projection operator approach [44,47,50,51].

The iterative optimization procedure used in the SP search typically starts near a local energy minimum representing the initial state of the magnetic system. The climb up to the SP involves two stages: (i) Escape from the convex region around the minimum, and (ii) convergence on a first-order SP using the GMMF technique. This two-stage procedure is to be repeated multiple times so as to identify, with some degree of confidence, all relevant SPs surrounding the given energy minimum. Convergence on various SPs is achieved by generating several different starting points near the energy minimum and/or by following different scenarios in the escape stage. For example, the convex region can be escaped by displacing the system from the initial state minimum along various eigenmodes of the system [44]. However, following the eigenmodes in the escape stage is not a requirement, as other strategies may also be used. In studies of atomic rearrangements, a method based on even distribution of points on a hypersphere in the configuration space has been used to sample different directions away from the initial state minimum [19,52,53]. Clearly, the choice of the escape strategy affects the efficiency of the method in finding as many distinct SPs as possible while keeping the number of the SP searches to a minimum. Choosing the optimal escape strategy is an important task which, however, goes beyond the scope of this study.

At a certain point during the escape stage, the minimum eigenvalue of the Hessian becomes negative, indicating that a basin of attraction for an SP [16] has been reached and that the convergence stage can be started. An efficient implementation of the GMMF method, used in the SP convergence stage, is the focus of this study. The steps involved in the GMMF calculations are summarized in the flowchart in Fig. 1(a).

In contrast to the escape stage, which can be organized in many different ways, the strategy for advancing the system during the convergence stage once the system is outside the convex region is more straightforward. The corresponding rotations of the magnetic moments are guided by a modified magnetic force designed so as to carry out a maximization of the energy along a certain direction, the inversion mode, and minimization along all orthogonal directions. Near an SP, the inversion mode necessarily is the minimum mode, i.e., the eigenvector of the Hessian corresponding to the lowest eigenvalue. However, near the boundary of the convex region, it can be advantageous to choose the inversion mode to be the Hessian's eigenvector corresponding to the second lowest eigenvalue or even higher eigenvalue. Such a formulation eventually results in a convergence on a first-order SP rather than a minimum. Specifically, the GMMF force on the ith magnetic moment in the system is defined as

$$\vec{f}_i = \vec{b}_i - (\vec{b}_i \cdot \vec{s}_i)\vec{s}_i, \tag{2}$$

where $\vec{s}_i$ is the unit vector in the direction of the ith magnetic moment and $\vec{b}_i$ is the effective field whose component along the inversion mode is reversed. The modified effective field $\vec{b}_i$ is defined by the following equation:

$$\vec{b}_i = -\vec{\nabla}_i E + 2(\boldsymbol{\nabla} E \cdot \boldsymbol{q})\vec{q}_i. \tag{3}$$

Here, $E = E(\boldsymbol{s})$ is the energy as a function of the magnetic configuration defined by vector $\boldsymbol{s} = (\vec{s}_1, \vec{s}_2, \ldots, \vec{s}_N)$, $\boldsymbol{q} = (\vec{q}_1, \vec{q}_2, \ldots, \vec{q}_N)$ is the unit vector representing the inversion mode, and $\boldsymbol{\nabla} = (\vec{\nabla}_1, \vec{\nabla}_2, \ldots, \vec{\nabla}_N)$, with $\vec{\nabla}_i \equiv \partial/\partial\vec{s}_i$. By construction, the GMMF force $\boldsymbol{f} = (\vec{f}_1, \vec{f}_2, \ldots, \vec{f}_N)$ is orthogonal to the magnetic moments, i.e., lies in the tangent space of $\mathcal{R}$ for a given magnetic configuration $\boldsymbol{s}$: $\boldsymbol{f} \in T_{\boldsymbol{s}}$ (see Fig. 2 for an illustration of the tangent space for a single magnetic moment).

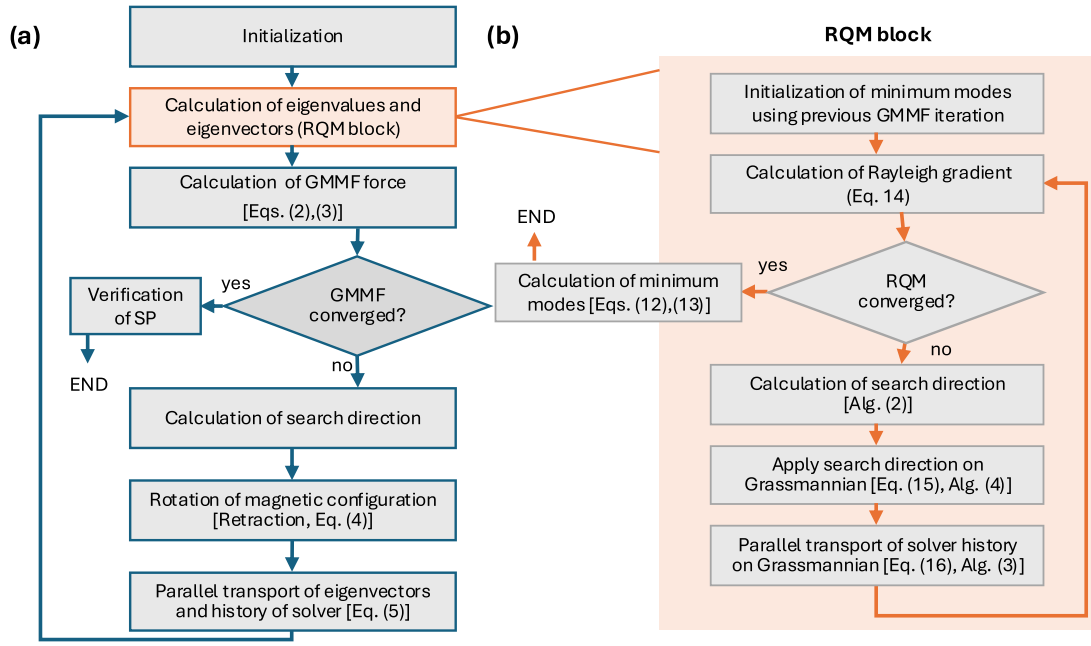

FIG. 1. Flowchart for the algorithm of the GMMF method (a) and for the Rayleigh quotient minimization (RQM) eigensolver method (b) as presented in Sec. II. In each GMMF iteration, the RQM block is executed to calculate the eigenvalues and eigenvectors of the Hessian for the current magnetic configuration. The pseudocode for the algorithms describing the RQM method is given in Appendix B.

The inversion along the minimum mode makes the effective field correspond to the neighborhood of a minimum of $E(\boldsymbol{s})$ rather than that of an SP. This is the basic idea of the method: a transformation of the problem of locating a first-order SP into the much simpler task of gradient-based minimization. In particular, the GMMF force is used to guide an iterative advancement of the magnetic structure toward an SP using some numerical optimization method, preferably one that accounts for the curvature of the configuration space $\mathcal{R}$ via retraction and parallel transport [54]. The concepts of retraction (movement on a manifold in a certain direction without leaving the manifold) and parallel transport (translation of geometrical data on a manifold) are implemented

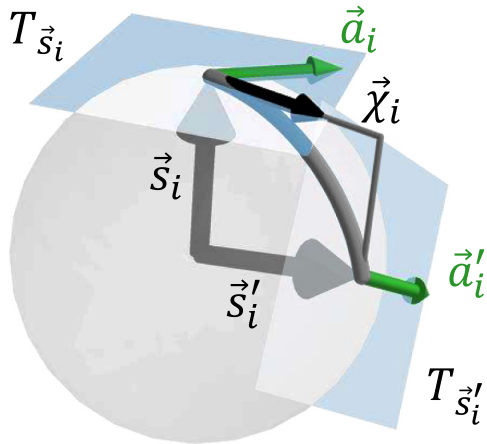

FIG. 2. Visualization of rotating a single magnetic moment $\vec{s}_i$ in the direction $\vec{\chi}_i \in T_{\vec{s}_i}$ (retraction). Also, the parallel transport of an exemplary vector $\vec{a}_i \in T_{\vec{s}_i}$ (green) towards the tangent space of the retracted magnetic moment $T_{\vec{s}_i'}$ is shown.

for magnetic systems via rotations and illustrated for a single magnetic moment in Fig. 2. Specifically, retracting a magnetic moment $\vec{s}_i$ in the direction $\vec{\chi}_i \in T_{\vec{s}_i}$, with $T_{\vec{s}_i}$ being the corresponding tangent space, to the updated position $\vec{s}_i'$ characterized by the tangent space $T_{\vec{s}_i'}$, as well as the parallel transport of a vector $\vec{a}_i$ (e.g., the gradient or search direction from previous iterations in optimization methods with memory) from $T_{\vec{s}_i}$ to $T_{\vec{s}_i'}$ can be computed using

$$\vec{s}_i' = D_{\vec{\chi}_i}(\varphi)\vec{s}_i, \tag{4}$$

$$\vec{a}_i' = D_{\vec{\chi}_i}(\varphi)\vec{a}_i. \tag{5}$$

Here, the 3×3 rotation matrix $D_{\vec{\chi}_i}(\varphi)$ is given by the Rodriguez rotation formula

$$D_{\vec{\chi}_i}(\varphi) = I + \sin\varphi_i K_{\vec{\chi}_i} + (1-\cos\varphi_i)K_{\vec{\chi}_i}^2, \tag{6}$$

where I is a 3×3 identity matrix and $\varphi_i = \varphi|\vec{\chi}_i|$ is the angle between $\vec{s}_i'$ and $\vec{s}_i$. The matrix $K_{\vec{\chi}_i}$ is given by

$$K_{\vec{\chi}_i} = \begin{pmatrix} 0 & -k_i^z & k_i^y \\ k_i^z & 0 & -k_i^x \\ -k_i^y & k_i^x & 0 \end{pmatrix}, \tag{7}$$

with k_i^x, k_i^y, k_i^z being the Cartesian components of the rotation axis $\vec{k}_i$:

$$\vec{k}_i = \vec{s}_i \times \frac{\vec{\chi}_i}{|\vec{\chi}_i|}. \tag{8}$$

The retraction and parallel transport on the configuration space $\mathcal{R}$ can be described by the direct sum of the 3×3

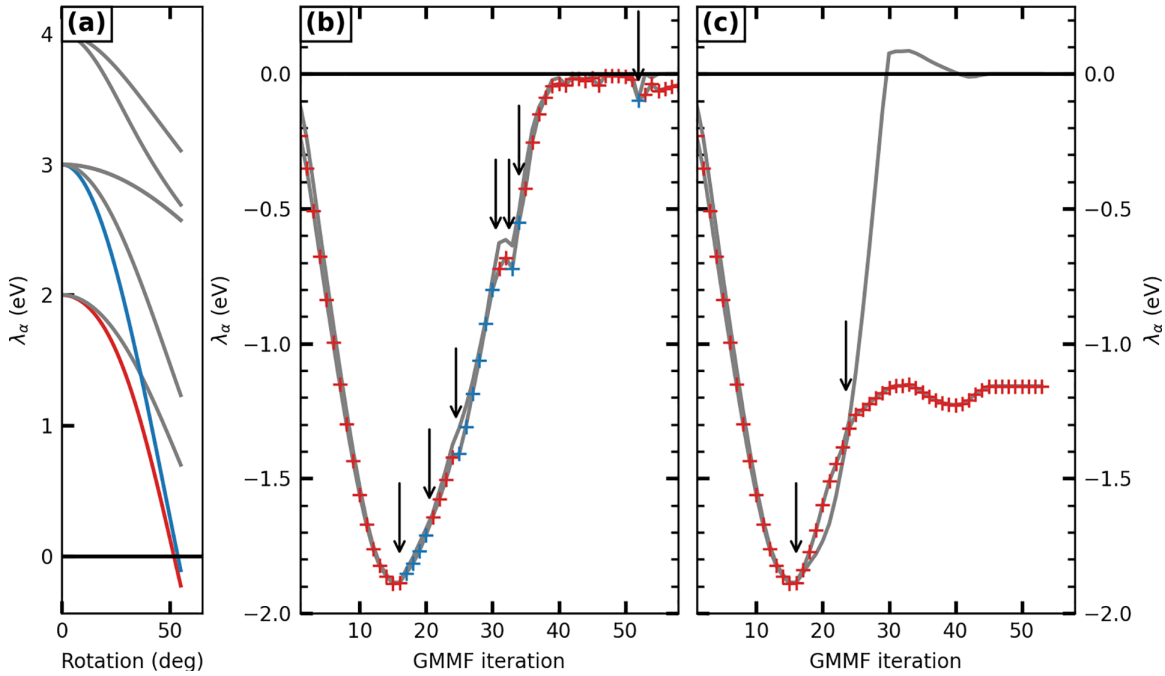

FIG. 3. SP search applied to the system of four magnetic moments described in Appendix A. (a) The lowest eigenvalues of the Hessian as functions of the angle of rotation of two moments with respect to the initial parallel-aligned state during the escape stage. The red and blue curves correspond to the modes that experience mode crossings during the convergence stage. The maximum rotation angle corresponds to the starting configuration used in the GMMF calculation during the convergence stage. The lowest eigenvalues are nearly equal at the maximum rotation angle. (b), (c) Evolution of the two lowest eigenvalues during the GMMF calculation, following two different strategies. The mode-crossing events are marked with black arrows. The color of the crosses codes the inversion mode. In (b), the inversion mode is always chosen to be the minimum mode. In (c), the definition of the inversion mode changes when a mode crossing occurs. In particular, the inversion mode corresponds to the Hessian's eigenvector associated with the second lowest eigenvalue between the mode-crossing events.

rotation matrices for the individual magnetic moments:

$$\mathcal{D}_{\boldsymbol{\chi}}(\varphi) = \begin{pmatrix} D_{\vec{\chi}_1}(\varphi) & 0 & \dots & 0 \\ 0 & D_{\vec{\chi}_2}(\varphi) & \dots & 0 \\ \vdots & \vdots & \ddots & \vdots \\ 0 & 0 & \dots & D_{\vec{\chi}_N}(\varphi) \end{pmatrix}. \quad (9)$$

While many different optimization algorithms can be used, we employ here a limited-memory Broyden-Fletcher-Goldfarb-Shanno (L-BFGS) solver [55] adapted to magnetic systems [56]. Typically, the calculation is considered to be converged when the magnitude of the GMMF force has dropped below some threshold value [see Fig. 1(a)]. After that, the candidate SP is verified by ensuring that one and only one eigenvalue of the Hessian is negative. Occasionally, following the GMMF force can lead back into the convex region around a minimum. This happens if the inversion mode becomes nearly orthogonal to the energy gradient. In this case, the GMMF optimization is essentially just an energy minimization with a displacement along the negative energy gradient. Such reentrance into the convex region can be detected when the lowest eigenvalue of the Hessian becomes positive, indicating the need to restart the SP search.

Calculating the GMMF force involves reversing the component of the effective field along the inversion mode. Typically, and always towards the end of the convergence stage, the inversion along the minimum mode is carried out. However, during GMMF optimization, a crossing of the two lowest eigenvalues and corresponding modes may occur. Such a situation is depicted in Fig. 3. The corresponding calculations were performed for a system with four magnetic moments described in Appendix A. In such a case, the use of only the minimum mode for the inversion at each iteration step leads to an abrupt change in the GMMF force. Most of the times, this does not cause problems and the method converges on an SP after the mode-crossing event. However, there are some situations where the two lowest modes are close to being degenerate and yet describe completely different changes in the magnetic structure. Then the use of only the minimum mode for the inversion may lead to repetitive mode-crossing events [see Fig. 3(b)]. In this case, the consistency between iteration steps is lost due to multiple abrupt changes in the GMMF force, preventing the optimization procedure from converging. By selecting the eigenvector corresponding to the second-lowest eigenvalue as the direction of inversion for several iterations after the mode-crossing event can help prevent this unwanted behavior [see Fig. 3(c)]. Inversion along several different modes can also increase the likelihood of identifying distinct SPs. It is, therefore, useful to calculate the two lowest modes, not just the minimum mode. Furthermore, it is necessary to calculate the second lowest eigenvalue in order to verify that the candidate SP is of first order, i.e., only the lowest eigenvalue of the Hessian is negative.

The evaluation of the Hessian eigenvectors corresponding to the two lowest eigenvalues needs to be carried out efficiently as it tends to be a computational bottleneck of

the GMMF method. Commonly used algorithms for finding the lowest few eigenvalues and corresponding eigenvectors include the Lanczos method [20] and extensions thereof, such as the Davidson method [21] and other even more sophisticated Krylov subspace algorithms [57]. In this work, we present an alternative approach where the lowest eigenpairs of the Hessian are obtained via the direct minimization of the generalized Rayleigh quotient. The high efficiency of the method is achieved by avoiding the evaluation of the full Hessian explicitly and by using the L-BFGS solver, adapted to account for the curvature of the Grassmann manifold on which the objective function is defined. A detailed description of the method is provided in the following subsections and the corresponding pseudocode presented in Appendix B.

A. Calculation of the two lowest modes using generalized Rayleigh quotient minimization

The two lowest modes, i.e., the eigenvectors corresponding to the two lowest eigenvalues of the Hessian, can be identified using the following Rayleigh quotient:

$$R(X) = \mathrm{tr}(X^T H X), \tag{10}$$

where H is the $2N\times 2N$ Hessian matrix and X is a $2N\times 2$ matrix whose columns are orthonormal vectors parametrizing all possible two-dimensional subspaces of the local tangent space of $\mathcal{R}$. The subspace containing the two lowest modes is spanned by the columns of X_{min} corresponding to a minimum of $R(X)$ [50]:

$$X_{\mathrm{min}} : R(X_{\mathrm{min}}) \rightarrow \mathrm{min}\,. \tag{11}$$

The representation of the two lowest modes $\boldsymbol{v}_\alpha$, $\alpha = 1, 2$, in the embedding $3N$-dimensional Euclidean space can be obtained from X_{min} using

$$\boldsymbol{v}_\alpha = U X_{\mathrm{min}} \tilde{\boldsymbol{v}}_\alpha, \tag{12}$$

where U is the projector onto the local tangent space of $\mathcal{R}$ and $\tilde{\boldsymbol{v}}_\alpha$ are the eigenvectors of the following 2×2 eigenvalue problem:

$$\left(X_{\mathrm{min}}^T H X_{\mathrm{min}}\right)\tilde{\boldsymbol{v}}_\alpha = \lambda_\alpha \tilde{\boldsymbol{v}}_\alpha, \quad \alpha \in \{1, 2\}. \tag{13}$$

The Rayleigh quotient minimization (RQM) needs to be performed at every iteration of the GMMF procedure. To achieve this, we have implemented an efficient method based on the L-BFGS solver equipped with the gradient of $R(X)$ on the Grassmann manifold [50]:

$$\nabla R(X) = 2[HX - X(X^T H X)]. \tag{14}$$

The pseudocode for the GMMF/RQM algorithm is presented in Appendix B. The RQM calculations are highly efficient and typically converge to X_{min} in just a few L-BFGS iterations, especially when the initial guess for X_{min} is taken from the solution of a previous GMMF iteration. In Sec. IV A, the performance of the GMMF/RQM approach is compared with that of an implementation of GMMF equipped with a state of the art extremal eigensolver based on a Krylov-Schur (KS) [58] method as implemented in the Intel Math Kernel Library [48] (GMMF/KS).

It is important to realize that the domain of $R(X)$ represents a curved, Grassmann manifold $G_{2N,2}$. Therefore, an efficient RQM requires implementation of retraction and parallel transport that adhere to the geometric constraints of $G_{2N,2}$. Given a search direction Λ for the current iteration X, the retraction to the next iteration X' on $G_{2N,2}$ must ensure orthonormality of the columns of X'. Here, we make use of the exponential map, which is a special kind of retraction following geodesics. On the Grassmann manifold, the action of the exponential map can be found by the compact singular value decomposition $\Lambda = P\Sigma V^T$ of the tangent vector Λ [50] (see Appendix B, Algorithm 4):

$$X' = XV\ \cos(\Sigma)V^T + P\ \sin(\Sigma)V^T. \tag{15}$$

The L-BFGS algorithm that we use for finding X_{min} approximates the second derivative of the Rayleigh quotient and combines information of the gradients and the search directions from the past few iterations. These history vectors are anchored in the tangent spaces of their point of calculation on the curved manifold. Thus, in each iteration of the RQM a history vector A has to be transported from the tangent space of X to the tangent space of X' using $A' = TA$ with [50]

$$T = (XV \quad P)\begin{pmatrix} -\sin\Sigma \\ \cos\Sigma \end{pmatrix} P^T + (I - PP^T), \tag{16}$$

where I is the $2N\times 2N$ identity matrix. A computationally efficient multiplication with this parallel transport matrix is given in Appendix B, Algorithm 3.

Finally, the global minimum of the Rayleigh quotient is given by X_{min} which spans the same subspace as the sought-for two eigenvectors of the Hessian. Note that all $2N\times 2$ matrices whose orthonormal columns span the same subspace represent the same point on $G_{2N,2}$. Thus, the eigenvectors corresponding to the two lowest eigenvalues of the Hessian are linear combinations of the columns of X_{min}, and are determined by solving Eq. (13).

A method for computing the Hessian for magnetic systems is described in Refs. [44,51] and is also summarized in Appendix C. Explicit evaluation of the Hessian is feasible for systems of moderate size and/or systems with only short-range interactions as the Hessian matrix then becomes sparse. The explicit Hessian is used in the KS implementation of the GMMF method.

The evaluation of the gradient of the Rayleigh quotient does not, however, require the explicit evaluation of the Hessian; only its action on X is needed [see Eq. (14)]. The action of the Hessian on X can be obtained through separate matrix-vector multiplications. These can be calculated using a finite-difference scheme for the energy gradient, as described in the following subsection. This approach avoids the explicit evaluation of the Hessian, providing a significant speedup in the GMMF calculations.

B. Action of the Hessian matrix

Calculation of the matrix-vector multiplication $H\boldsymbol{x}$, where $\boldsymbol{x}$ is a column of X, is needed for the gradient-based minimization of the Rayleigh quotient [see Eq. (14) for $\nabla R(X)$]. It can be performed without the explicit evaluation of the Hessian H using a finite-difference scheme for the energy gradient. In such a scheme, one needs to take into account the curvature of the configuration space. In particular, energy

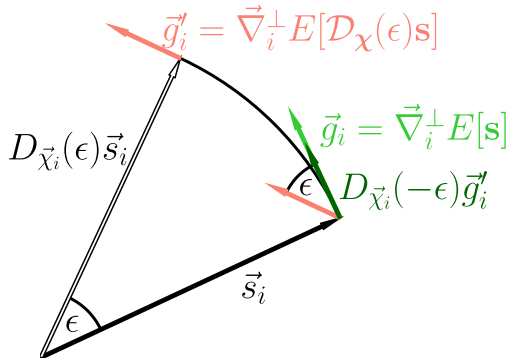

FIG. 4. Illustration of the quantities involved in calculating the action of the Hessian by forward finite-difference approximation with a displacement parameter ϵ for a single magnetic moment $\vec{s}_i$. To calculate the finite difference of the gradient $\vec{g}_i$ along a given direction, the magnetic moment is first retracted (rotated) along this direction and the gradient $\vec{g}_i'$ is calculated for the rotated magnetic moment $D_{\vec{\chi}_i}(\epsilon)\vec{s}_i$. Parallel transport $[D_{\vec{\chi}_i}(-\epsilon)\vec{g}_i']$ is then applied towards the tangent space of the initial magnetic moment $\vec{s}_i$ to ensure that both gradients are defined within the same tangent space for the calculation of the finite difference.

gradients for retracted magnetic configurations must be parallel transported to the location of the current magnetic configuration so as to be anchored in the same tangent space (see Fig. 4). The retraction and parallel transport are implemented through rotations [see Eqs. (4) and (5)] in the direction of $\boldsymbol{x}$, which can be expressed in terms of the vector $\boldsymbol{\chi}$ in the embedding $3N$-dimensional Euclidean space, thereby avoiding basis changes:

$$\boldsymbol{\chi} = U\boldsymbol{x}. \tag{17}$$

The forward finite-difference scheme for computing $H\boldsymbol{x}$ is used:

$$H\boldsymbol{x} \approx U^T \frac{\mathcal{D}_{\boldsymbol{\chi}}(-\epsilon)\nabla^{\perp}E[\mathcal{D}_{\boldsymbol{\chi}}(\epsilon)\boldsymbol{s}] - \nabla^{\perp}E[\boldsymbol{s}]}{\epsilon}. \tag{18}$$

Here, $\nabla^{\perp} = (\vec{\nabla}_1^{\perp}, \ldots, \vec{\nabla}_N^{\perp})$, with $\vec{\nabla}_i^{\perp} = \vec{\nabla}_i - \vec{s}_i(\vec{s}_i \cdot \vec{\nabla}_i)$, $\epsilon > 0$ is the displacement parameter, and projector U^T yields the $2N$-dimensional representation of the action of the Hessian matrix as required in the context of the RQM algorithm. Note that the angle of rotation is not uniform across the entire system. Instead, it is defined individually for each magnetic moment based on the components of $\boldsymbol{\chi}$ [see Eqs. (6)–(9)]. The optimal value of the displacement parameter ϵ yielding the minimum error of the finite difference was determined using the Richardson extrapolation scheme [59–61] with the initial ϵ value of 10^{-6}. If necessary, the finite-difference scheme can be extended to incorporate additional stencil points. However, this increases computational cost, as each additional point requires extra parallel transport and retraction operations. We find that the forward (or, equivalently, backward) finite-difference scheme, in which these operations are performed only once, combined with Richardson extrapolation, provides a good balance between accuracy and computational efficiency of the RQM calculations.

C. Further analysis

The GMMF/RQM method offers various synergies with other approaches, as listed below. On the one hand, it is straightforward to generate the MEP once a first-order SP and the corresponding unstable mode have been determined. To achieve this, a steepest descent path is generated from the SP on both sides toward the stable states. During the minimization, the cumulative geodesic distance can be used to control how many points are generated to provide a good discrete representation of the MEP, similar to the path that would be obtained by the GNEB method if both initial and final state minima were known beforehand.

On the other hand, the highest-energy image of a partially converged GNEB calculation can be used as a starting point for a GMMF calculation. In this way, the fast convergence of the GMMF method on a first-order SP is used instead of the larger computational effort of converging all images in a GNEB simulation.

Once an SP has been found, the preexponential factor in the rate constant for the corresponding transition can be obtained within the harmonic transition state theory (HTST) approximation [23]. By identifying all relevant, low-energy SPs connecting to a given initial state, a Monte Carlo procedure can be used to select which transition will occur next in a long timescale evolution of the system, as has been done for atomic systems in the adaptive kinetic Monte Carlo method [8] where the system recursively traverses from one energy minimum to another *via* the identified SPs. Such a long timescale simulation at a finite temperature, combined with systematic coarse graining of the energy landscape [62,63], can be the basis for simulated annealing search for the global energy minimum representing the most stable state of the system.

III. MODEL

The GMMF/RQM method described in Sec. II can be applied to any system where the energy depends on the orientation of magnetic moments $\boldsymbol{s}$, such as atomistic spin models [64]. One example is the extended Heisenberg model which has been extensively used to describe various topological spin textures such as magnetic skyrmions and other even more complicated magnetic states [35,65], including those containing Bloch points [37,38,66].

To demonstrate the GMMF/RQM method, we use the following Hamiltonian on square (see Sec. IV A) and cubic lattice (see Sec. IV B, Appendix E) models:

$$E = -J\sum_{i,j}\vec{s}_i \cdot \vec{s}_j - D\sum_{i,j}\hat{d}_{ij} \cdot (\vec{s}_i \times \vec{s}_j) - \mu\sum_i \vec{B} \cdot \vec{s}_i + \eta E_{\text{mag}}. \tag{19}$$

Nearest-neighbor exchange (J) is included as well as nearest-neighbor Bloch-type Dzyaloshinskii-Moriya interaction (DMI) (D), with the unit DMI vector $\hat{d}_{ij}$ oriented along the connection line of the interacting magnetic moments i and j. The magnitude of the magnetic moments is set to $\mu = 1\,\mu_B$, with μ_B being the Bohr magneton. An external magnetic field $\vec{B}$ is applied in the z direction. The last term in Eq. (19)

TABLE I. Parameters of the extended Heisenberg model [Eq. (19)] used in the calculations. The size refers to the number of magnetic moments in the x, y, and z directions, respectively. For the first application, a range in parameter values was explored. The magnetic moment is $\mu = 1\mu_B$ and the exchange parameter is $J = 1$ meV for all calculations. The explicit calculation of magnetostatics using a lattice constant of 3 Å is controlled by the parameter η in Eq. (19). The 3D system employs periodic boundary conditions along the x and y directions and open boundaries in the z direction. For the monolayer system, open boundary conditions are applied along all spatial directions.

System size	Section	Explicit magnetostatics	D (meV)	B (T)
50×50×1	IV A	no	0.2–0.8	2.0–5.0
32×32×32	IV B	yes	0.45	2.8
32×32×32	Appendix E	no	0.45	2.8

represents the magnetostatic interaction whose energy E_{mag} is computed using the fast Fourier transform [67,68]. The parameter $\eta = 0, 1$ is used to either activate ($\eta = 1$) or deactivate ($\eta = 0$) explicit treatment of magnetostatics. The values of all parameters are listed in Table I.

Magnetostatic interaction is not explicitly considered in the monolayer system studied in Sec. IV A, both for consistency with the study by Müller *et al.* [44] and because magnetostatics can effectively be reduced to a local anisotropy in this case [69]. In contrast, magnetostatics is explicitly included in the 3D system analyzed in Sec. IV B. In that case, the values of J, D, and B are chosen to match those in Ref. [37] and a lattice constant of 3 Å is used. The size of the monolayer system is 50×50×1 magnetic moments, while the 3D system has a size of 32×32×32 moments. The 3D system employs periodic boundary conditions along the x and y directions and open boundary conditions along the z direction. Open boundary conditions are applied along all spatial directions for the monolayer system. For comparison, we also consider in Appendix E a 3D system without magnetostatics, identical to the one studied in Ref. [37].

IV. RESULTS

A. Skyrmion collapse mechanisms

In this section, the application of the GMMF method to systems hosting skyrmions is demonstrated. The energy-minimum skyrmion state [see Fig. 5(a)] serves as a starting configuration for the SP searches. For $J = 1$ meV, $D = 0.55$ meV, and $B = 3.1$ T, four distinct SPs corresponding to different skyrmion collapse mechanisms can be identified using the GMMF method:

(1) $\mathrm{SP_{rad}}$ corresponding to a Bloch pointlike configuration [Fig. 6(c)] on the path that connects the skyrmion state with the FM state via radially symmetric shrinking of the skyrmion.

(2) $\mathrm{SP_{esc}}$ characterizing the collapse of the skyrmion via an escape through the boundary of the system [Fig. 6(d)]. The SP configuration is a dropletlike deformed skyrmion attached to the system's boundary.

(3) $\mathrm{SP_{dup}}$ corresponding to the splitting of a single skyrmion into two skyrmions (skyrmion duplication). The SP configuration is an eight-shaped deformed skyrmion [Fig. 6(b)].

(4) $\mathrm{SP_{bag}}$ characterizing the transformation of the skyrmion state into the skyrmion bag state [Fig. 6(a)].

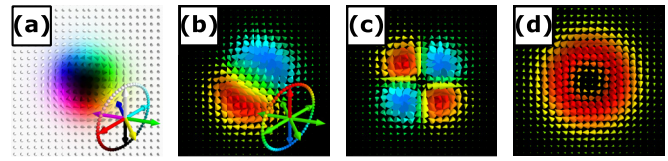

FIG. 5. (a) Skyrmion corresponding to a local energy minimum on a square lattice with $J = 1$ meV, $B = 3.1$ T, and $D = 0.55$ meV [see Eq. (19)]. The inset explains the hue-saturation-lightness color scheme. While the azimuthal angle of the magnetic moments is represented by the hue, the lightness encodes the polar angle of the magnetic moments for a fixed saturation of 1.0. (b)–(d) Vector field representation of the Hessian eigenvectors corresponding to the translation (a), elongation (b), and breathing (c) modes. The color codes the polar angle of the eigenvector components [see inset in (b)].

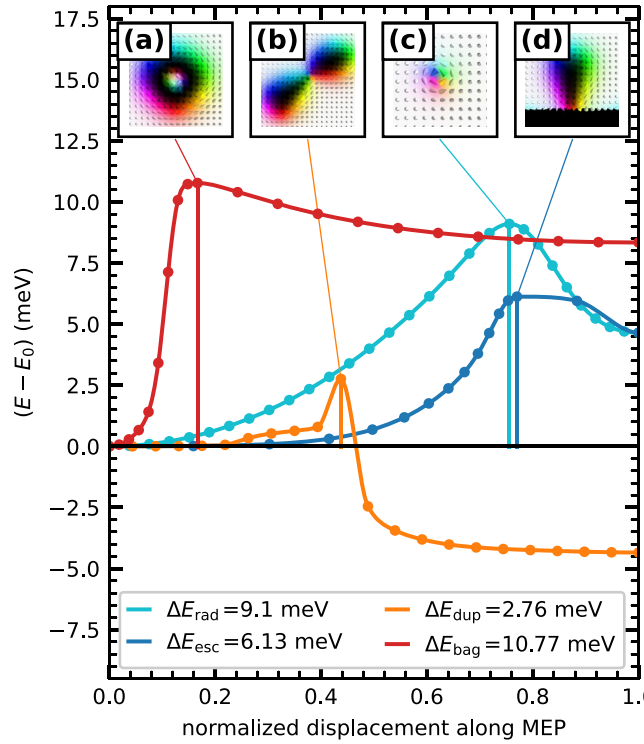

FIG. 6. Energy variation along MEPs for skyrmion collapse, shown relative to the skyrmion energy E_0, as obtained by CI-GNEB calculations for the monolayer system with $J = 1$ meV, $B = 3.1$ T and $D = 0.55$ meV [see Eq. (19)]. The initial paths were generated using the SP configurations obtained with the GMMF algorithm (see Sec. II C). The insets show the first-order SP configurations for the transition of the skyrmion into the skyrmion bag (a), the duplication of a skyrmion (b), the radially symmetric skyrmion collapse (c), and the escape of the skyrmion through the system boundary (d). The energy barriers defined as the energy difference between the SP state and the skyrmion state are represented by vertical lines, with their values provided in the legend.

The SP configuration is a skyrmion with strongly canted magnetic moments at the skyrmion center.

Each of these SPs corresponds to the configuration of highest energy of the MEP connecting the skyrmion state with the FM state, the skyrmion bag state, or the state of two skyrmions. The MEPs are shown in Fig. 6. They were obtained from CI-GNEB calculations where an initial path was generated by sliding down the energy surface from the SP on both sides toward the stable states (see Sec. II C). For the selected values of the Hamiltonian parameters, the energy of the ferromagnetic state is higher than the energy of the isolated skyrmion, and the energy of two skyrmions is the lowest.

To locate the four SPs, the convex region of the skyrmion energy minimum is escaped using four different strategies. Each strategy corresponds to a specific deformation of the magnetic configuration, thereby introducing tendencies that reflect the shape of the SP configurations. Three of the four deformations are generated using eigenvectors from the low-curvature part of the skyrmion state's eigenvalue spectrum. In this case, the sparsity of the Hessian and the moderate system size make it feasible to explicitly construct the Hessian matrix and compute the eigenvectors using standard methods. Specifically, we used the Krylov-Schur solver as implemented in the Intel Math Kernel Library [48] to perform the eigenvector computations. The results are shown in Figs. 5(b)–5(d), and the corresponding modes have been discussed in several previous publications [44,51,70–72]. While SP_{bag} should, in principle, be reachable by combining several modes, here a simple rotation of the magnetic moments at the skyrmion center is used instead to generate the appropriate deformation. At the end of the escape stage, a suitable configuration for initiating the subsequent GMMF stage is obtained, characterized not only by at least one negative eigenvalue, but also by the corresponding eigenvector used for inversion with a significant component along the force direction, which reduces the likelihood of the system returning to the convex region. To test the sensitivity of the GMMF method to the choice of the starting point, six such initial configurations $\mathcal{I}_1$–$\mathcal{I}_6$ were selected for each collapse mechanism [see black diamonds in Figs. 7, 8(a), and 9(a)]. These configurations differ in their distance from the convex region around the skyrmion-state minimum, yet all converge to the same SP associated with the respective mechanism, as described below.

Iteratively displacing the skyrmion configuration along the eigenvector of the breathing mode [see Fig. 5(d)] shrinks or expands the skyrmion. Figure 7(a) shows how several of the lowest eigenvalues change as the skyrmion shrinks. At some point, one of the eigenvalues rapidly decreases and turns negative indicating that the convex region around the skyrmion-state minimum has been escaped. A subsequent application of GMMF leads to SP_{rad}. A similar displacement along one of the two skyrmion translational modes [see Fig. 5(b)] induces a tendency for the skyrmion escape through the edge of the system. As the skyrmion approaches the edge, the open boundaries lift the degeneracy between the translational modes. The eigenvalue associated with the mode corresponding to motion orthogonal to the one being followed becomes negative earlier. Still, it is appropriate to continue following the initially selected mode to bring the skyrmion

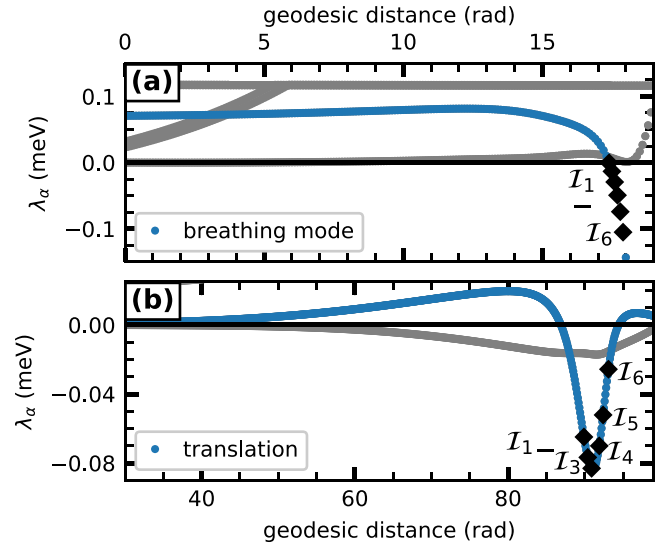

FIG. 7. Evolution of the lowest eigenvalues of the Hessian during iterative displacement along the breathing mode (a) and the translation mode (b) starting from the skyrmion state. The cumulated geodesic distance along this displacement is shown on the x axis. The black diamonds $\mathcal{I}_1$–$\mathcal{I}_6$, corresponding to six different starting configurations for the GMMF method, indicate the eigenvalues associated with the inversion mode. The parameters of the Hamiltonian are $J = 1$ meV, $B = 3.1$ T, and $D = 0.55$ meV.

closer to the edge of the system and steer the magnetic configuration toward SP_{esc}. Eventually, this mode becomes the minimum mode [see Fig. 7(b)]. The corresponding configurations mark suitable initial points for finding SP_{esc} using GMMF.

To induce a tendency toward SP_{dup}, the escape stage begins by following one of the two skyrmion elongation modes [see Fig. 5(c)]. However, elongation alone is insufficient to produce a suitable starting point for convergence to SP_{dup}. Additional local narrowing of the elongated skyrmion is required during the escape stage. This deformation can be induced by switching to a corresponding mode that emerges in the low-curvature part of the spectrum while the elongation mode is being followed. From that point onward [Fig. 8(a)], following the narrowing mode causes the eigenvalue associated with another mode to decrease rapidly, eventually making that mode the minimum mode. Once this occurs, a configuration is selected as the starting point for the GMMF simulation, which then converges to SP_{dup}. Note that in this case, the inversion mode does not coincide with any of the modes used during the escape stage.

The escape strategy for SP_{bag} is not based on the displacement along eigenmodes of the skyrmion, which is in contrast to other SPs. Instead, the magnetic moments at the skyrmion center are rotated toward the direction of the applied magnetic field. This is schematically shown in the inset in Fig. 9(a). During this deformation, one of the eigenvalues begins to decrease rapidly and eventually becomes the lowest eigenvalue. At this point, the application of the GMMF method leads to the identification of SP_{bag}.

Realization of various additional deformations during the escape stage did not lead to the identification of any further

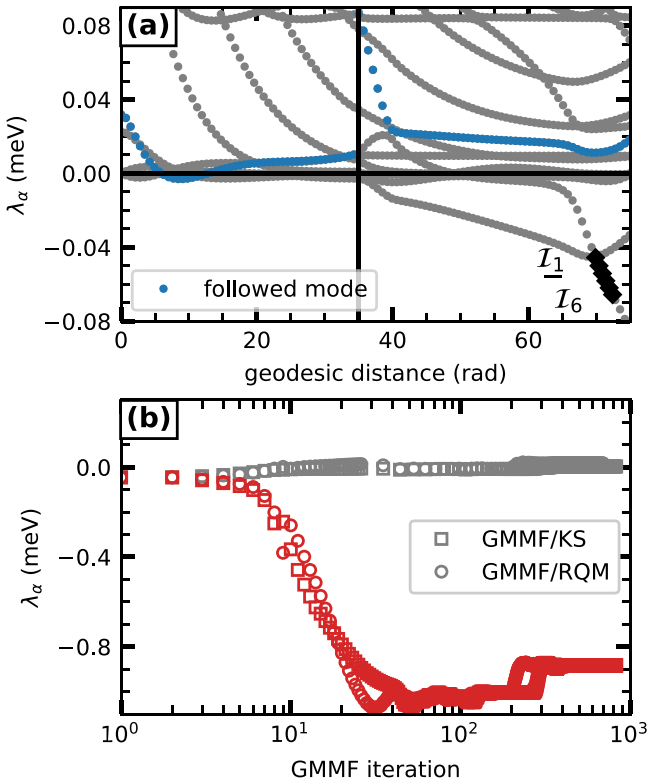

FIG. 8. (a) The evolution of the lowest eigenvalues of the Hessian during the escape stage corresponding to iterative displacement of the system along the skyrmion elongation mode (before the black vertical line) and the mode describing a narrowing of the central part of the elongated skyrmion (after the black vertical line). The black diamonds $\mathcal{I}_1$–$\mathcal{I}_6$, corresponding to six different starting configurations for the GMMF method, indicate the eigenvalues associated with the inversion mode. (b) The evolution of the two lowest eigenvalues during the application of the GMMF/RQM and GMMF/KS methods for the starting point $\mathcal{I}_1$. The final configuration of the GMMF algorithm corresponds to $\mathrm{SP}_{\mathrm{dup}}$. The parameters of the Hamiltonian are $J = 1$ meV, $B = 3.1$ T, and $D = 0.55$ meV.

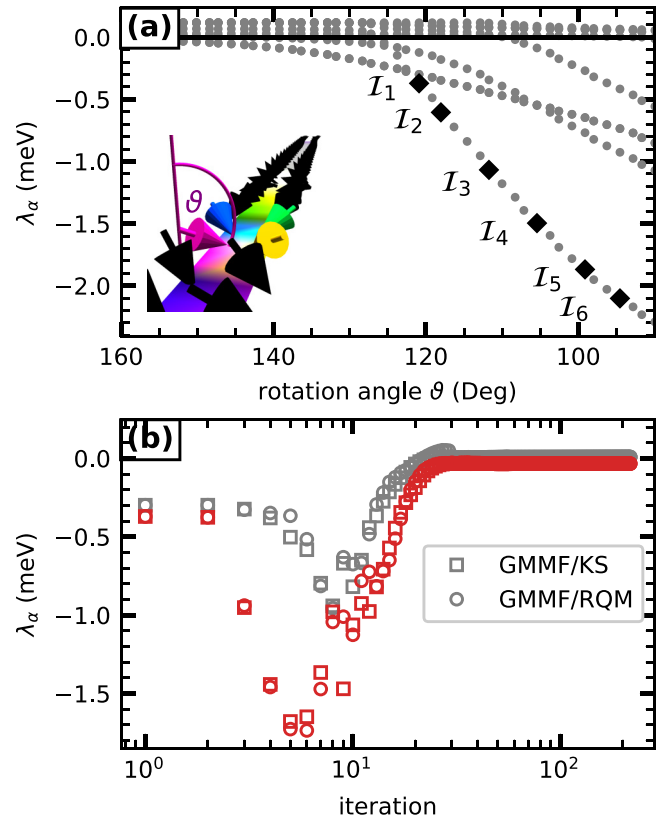

FIG. 9. (a) The evolution of the lowest eigenvalues of the Hessian during the uniform rotation of the four magnetic moments in the core of the skyrmion. The angle between the magnetic moment and the z axis is ϑ, while the in-plane component of the magnetic moments always points towards the center of the skyrmion. The black diamonds $\mathcal{I}_1$–$\mathcal{I}_6$, corresponding to six different starting configurations for the GMMF method, indicate the eigenvalues associated with the inversion mode. (b) The evolution of the two lowest eigenvalues during the application of the GMMF/RQM and GMMF/KS methods for the starting point $\mathcal{I}_1$. The final configuration of the GMMF algorithm corresponds to $\mathrm{SP}_{\mathrm{bag}}$. The values of the Hamiltonian parameters are $J = 1$ meV, $B = 3.1$ T, and $D = 0.55$ meV.

SPs. In particular, following the skyrmion triangular deformation mode, which induces a tendency toward skyrmion "triplication," causes the GMMF procedure to return to the convex region of the energy surface and the corresponding "triplication" SP is not identified. Physical arguments also suggest that the "triplication" SP, or other SPs associated with transitions involving a change in the system's topological charge by more than one, are either improbable or inaccessible due to their likely very high energy. In skyrmionic systems, the magnetic transitions reported so far involve no change in topological charge or a change by one, with the latter mediated by SPs involving high-energy Bloch pointlike defects. Changing the topological charge by an amount greater than one would likely require an even higher-energy configuration with either several such defects or a new type of defect capable of inducing such a change in the topological number, both of which seem unlikely.

The evolution of the two lowest eigenvalues during the application of the GMMF method equipped with the RQM eigensolver (GMMF/RQM) is shown in Fig. 8(b) for $\mathrm{SP}_{\mathrm{dup}}$ and in Fig. 9(b) for $\mathrm{SP}_{\mathrm{bag}}$. For comparison, the same results are depicted for a GMMF method using the Krylov-Schur eigensolver. One can identify slight differences between the eigenvalues obtained in GMMF/RQM and GMMF/KS. This is expected due to the qualitative difference between the RQM and KS eigensolvers leading to slightly different search directions on the energy landscape. Accordingly, the eigenspectrum is not determined at exactly the same point in configuration space in the following iteration. Therefore, the GMMF method is stable against a slight variation of the optimization path, which is underlined by the behavior shown in Figs. 8(b) and 9(b) as both methods converge reliably on the same SP.

Figure 9(b) illustrates that the lowest and second-lowest eigenvalues can approach each other closely during GMMF calculations. This places a requirement on the eigensolver to be able to resolve spectra that are nearly degenerate, and the RQM method successfully meets this requirement in all situations encountered here.

TABLE II. The mean wall time τ and the number of iterations κ required to find SPs describing skyrmion transformations using the GMMF/RQM method, as ratios of those required using the GMMF/KS method.

	SP_{rad}		SP_{esc}		SP_{dup}		SP_{bag}	
Initial point	τ	κ	τ	κ	τ	κ	τ	κ
$\mathcal{I}_1$	0.14 ± 0.04	1.18	0.08 ± 0.05	1.50	0.05 ± 0.02	0.83	0.12 ± 0.04	1.73
$\mathcal{I}_2$	0.14 ± 0.04	1.07	0.10 ± 0.05	2.05	0.06 ± 0.03	1.02	0.13 ± 0.04	1.84
$\mathcal{I}_3$	0.14 ± 0.05	1.10	0.10 ± 0.04	1.93	0.04 ± 0.02	0.80	0.14 ± 0.04	1.89
$\mathcal{I}_4$	0.14 ± 0.05	1.09	0.11 ± 0.04	2.09	0.05 ± 0.03	0.92	0.10 ± 0.04	1.22
$\mathcal{I}_5$	0.14 ± 0.04	1.14	0.10 ± 0.04	1.97	0.06 ± 0.04	1.02	0.11 ± 0.05	1.45
$\mathcal{I}_6$	0.13 ± 0.05	1.06	0.06 ± 0.04	1.09	0.04 ± 0.03	0.82	0.11 ± 0.04	1.42

In order to get an impression of how the performance of the GMMF/RQM method compares to a straightforward implementation of the GMMF method equipped with a state-of-the-art eigensolver from the widely used Intel Math Kernel Library, we compare the wall times required by each implementation of the GMMF to achieve convergence on the four targeted SPs. The wall time (averaged over 50 runs) and the number of iterations until convergence of the GMMF/RQM and GMMF/KS methods for each starting configuration and SP are provided in Table II. The GMMF/RQM is on average 10 times faster, although a slightly longer path is followed on the energy surface resulting in a small increase in the number of iterations. Comparison of the computational efficiency of the RQM and KS eigensolvers is not straightforward. The RQM method benefits significantly from using finite differences of the gradients instead of explicitly calculating the Hessian, even when the Hessian is sparse. Furthermore, it is not clear how the convergence behavior of an L-BFGS optimization of the Rayleigh quotient compares to the KS method. A detailed analysis of this will be done in the future.

Note also that we do not restrict the application of the GMMF algorithm to regions of the configuration space where one and only one eigenvalue is negative. Such points can be hard to find especially in high-dimensional systems. Therefore, we allow for starting points where multiple eigenvalues are negative. As the energy is minimized along all directions orthogonal to the inversion mode, only one eigenvalue becomes negative at some point.

The efficiency of the GMMF/RQM method in locating SPs enables the straightforward identification of the domains in the parameter space where particular transition mechanisms exist, analogous to how magnetic phase diagrams are constructed by energy minimization. The domains of existence for SP_{rad}, SP_{esc}, SP_{dup}, SP_{bag}, along with those for the corresponding energy minima, are shown in Fig. 10. They were obtained by varying the B and D parameters and performing GMMF/RQM calculations for each point in the parameter space. Each calculation was initialized using the SPs determined for $B = 3.1$ T and $D = 0.55$ meV. For parameter values outside the domains shown in Fig. 10, all GMMF calculations either converge to SPs unrelated to the corresponding domain or return to the convex region near a local minimum.

SP_{rad} is present as long as the skyrmion state and the FM state coexist [see Figs. 10(a) and 10(b)]. Interestingly, the domains of existence for SPs do not always coincide with those of the adjacent energy minima. For example, the escape mechanism is not always available as the domain for SP_{esc} is smaller than that for SP_{rad} [see Figs. 10(b) and 10(c)]. At large D values, where the isolated skyrmion remains metastable and its radial collapse is still possible, the skyrmion tends to elongate as it approaches the system boundary, forming an intermediate metastable state rather than escaping directly through the boundary [73]. Similarly, SP_{dup} is only present in the part of the skyrmion domain with large DMI [see Figs. 10(a) and 10(d)], although duplication of a skyrmion is always possible through the emergence of a second skyrmion from the FM background via SP_{rad}. Finally, SP_{bag} is limited to a very narrow region in the parameter space [see Fig. 10(e)].

The energy barrier for each skyrmion transformation can be obtained from the energy difference between the skyrmion state and the corresponding SP. Figure 10(f) shows how the energy barriers for each transition mechanism depend on the external magnetic field for a fixed DMI strength, $D = 0.5$ meV.

B. Collapse mechanisms of 3D magnetic states

The advantage of using the finite-difference scheme in the GMMF method becomes particularly evident for large systems with long-range interactions, where building the full Hessian would be prohibitively expensive in terms of time and memory. This is demonstrated through the application of the GMMF/RQM method to a system of $32\times32\times32$ magnetic moments, where the magnetostatic interaction is explicitly included. For the chosen interaction parameters (see Table I), the conical phase is the ground state of the system. However, skyrmion tubes and chiral bobbers [37], skyrmion tubelike spin textures that extend from the surface into the bulk and terminate at a Bloch point, can also exist as metastable states. Here, we demonstrate how the GMMF/RQM method can locate SPs in this system, providing insight into the mechanisms of transitions between different magnetic configurations and even revealing previously unknown metastable textures. Notably, significant results can be obtained without performing an escape stage, as demonstrated in the following.

Specifically, we initialize the system with a cylindrical region of randomly oriented magnetic moments embedded in the conical phase [see Fig. 11(a)]. The cylinder's diameter is set to be roughly the modulation period of the conical phase, an expected size scale for magnetic textures in this material. Since the initial state lies far from any energy minimum, it is outside the convex region of the energy landscape, and the escape stage becomes unnecessary. Thus, the GMMF optimization can start directly from this state. An example of

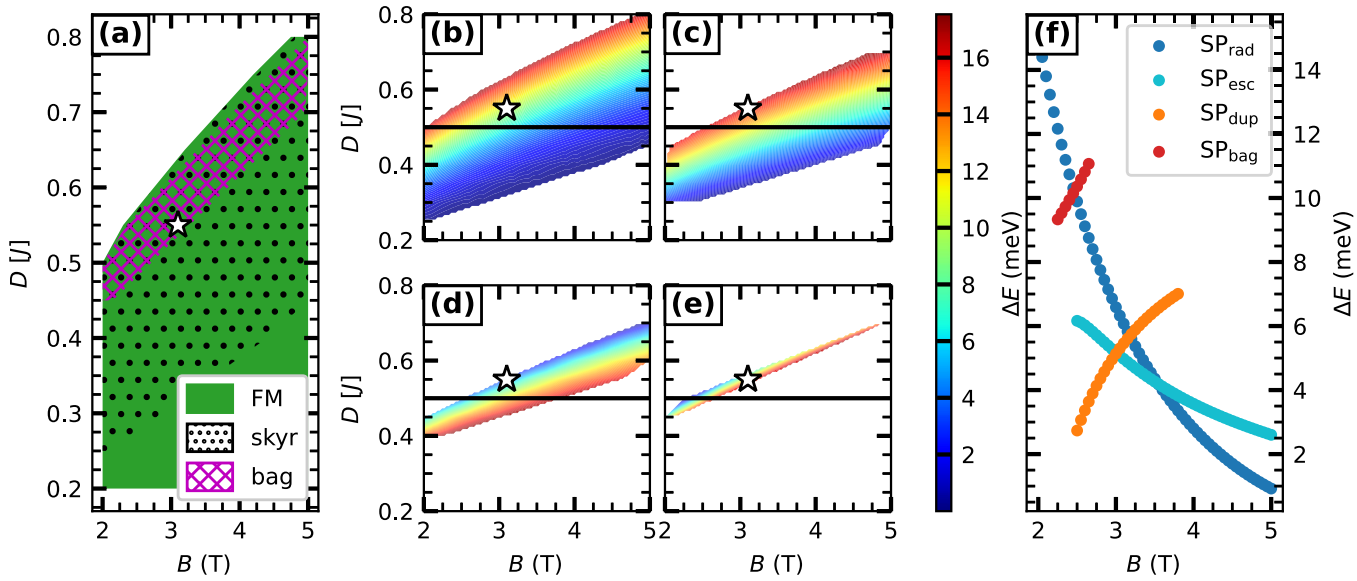

FIG. 10. (a) Parameter domains of metastability of the ferromagnetic state (FM), the skyrmion (skyr), and the skyrmion bag (bag) obtained by energy minimization initiated with the corresponding states for the parameters $B = 3.1$ T and $D = 0.55$ meV (star symbol). The white area corresponds to the domain where all minimizations yield the spin spiral state. (b)–(e) Existence diagrams for the SPs SP_{rad}, SP_{esc}, SP_{dup}, and SP_{bag} obtained via the GMMF/RQM method initialized with the corresponding SP at $B = 3.1$ T and $D = 0.55$ meV (star symbol). The color map represents the energy barrier ΔE which is the difference of the energy of the SP and the energy of the skyrmion. (f) The energy barriers ΔE as functions of the applied magnetic field for a constant DMI parameter $D = 0.55$ meV [horizontal lines in (b)–(e)].

such a GMMF calculation is illustrated in Fig. 11. Although multiple negative eigenvalues of the Hessian are present at the beginning of the optimization, the GMMF method brings the system to a valley characterized by a single negative eigenvalue and eventually converges on a first-order SP corresponding to the magnetic configuration shown in Fig. 11(b). Multiple mode-crossing events occur during the optimization process. These crossings appear as cusps in Fig. 11(c), which shows the evolution of the two lowest eigenvalues during the GMMF calculation. In each mode-crossing event, the minimum mode is consistently chosen as the inversion direction.

A small displacement from the SP along the unstable mode, followed by energy minimization, reveals two adjacent energy minima corresponding to the skyrmion tube and the chiral bobber [see Figs. 11(d) and 11(e)]. This illustrates a mechanism for skyrmion tube collapse via detachment of its end from the surface and the formation of a single chiral bobber.

Interestingly, the chiral bobber shown in Fig. 11 and inset i of Fig. 12 is significantly longer than the one originally reported in Ref. [37]. The elongated bobber remains a metastable state even when magnetostatic interactions are excluded (see Appendix E). Further analysis shows that the elongated chiral bobber corresponds to a relatively shallow energy minimum. Displacing the Bloch point by one lattice constant toward the base of the bobber and applying the GMMF method reveals a nearby SP only slightly higher in energy. Following the steepest descent path from this SP yields an MEP corresponding to the contraction of the bobber. The MEP terminates at a shorter chiral bobber, consistent with the typical length reported in Ref. [37] (see inset v in Fig. 12). The energy profile along this MEP exhibits a steplike structure, with each step associated with a reduction of the bobber length by one lattice constant (see Fig. 12). However, no intermediate energy minima are formed during this process.

Performing around 500 GMMF simulations from different initial states similar to that shown in Fig. 11(a) yields a variety of SPs, although different simulations often converge to the same configuration. For each SP, we construct an MEP by following steepest descent paths in both directions. Interestingly, MEPs originating from different SPs sometimes terminate at the same energy minima, thereby revealing connections between distinct metastable configurations. In this way, the set of identified SPs, minima, and corresponding MEPs maps out the network of transitions between metastable states. The resulting network describes various mechanisms for the decay of a skyrmion tube into the conical phase, as illustrated in Fig. 12. This transformation may proceed through various intermediate states, including combinations of chiral bobbers and coupled Bloch point pairs known as chiral globules [38].

In addition to the detachment of the skyrmion tube from the surface, GMMF calculations reveal another collapse mechanism that corresponds to a lower-energy barrier: the rupture of the skyrmion tube, followed by the formation of two chiral bobbers at opposite surfaces of the system. This second mechanism was also identified by Rybakov *et al.* [37] using the GNEB method. In our case, however, depending on the rupture point, either both bobbers or only one may appear elongated; the latter scenario is shown in Fig. 12, inset ii. From this state, the transition to the conical phase can follow several pathways. One involves the detachment of a chiral globule from an elongated bobber, forming a metastable complex consisting of two chiral bobbers and a globule (see inset iii in Fig. 12). The system eventually reaches the conical phase through the sequential collapse of the individual com-

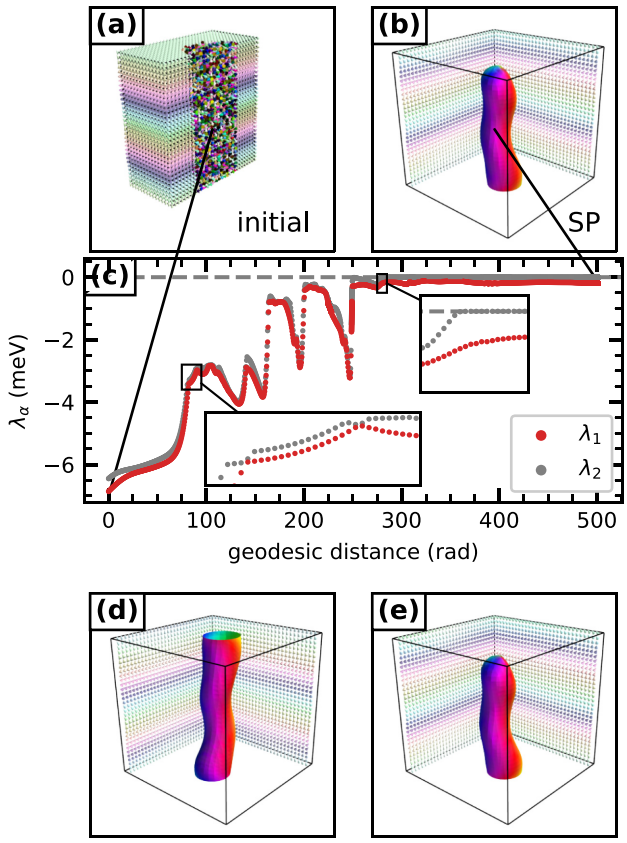

FIG. 11. An example of GMMF calculations applied to a 3D system. (a) Starting configuration represented by a cylindrical region of randomly oriented magnetic moments embedded in the conical phase. (b) The SP configuration to which the GMMF method converges. (c) The lowest (λ_1, red) and the second-lowest (λ_2, gray) eigenvalues of the Hessian of the energy as functions of the cumulative displacement of the system in the configuration space during the GMMF optimization. The left bottom inset shows a mode-crossing event. The right top inset highlights that one and only one eigenvalue is negative at the end of the optimization and thus the final state represents a first-order SP. (d), (e) Metastable configurations adjacent to the SP shown in (b). The orientation of magnetic moments is indicated by color, as described in Fig. 5(a). For (b), (d), and (e), the isosurfaces of $s_z = 0$ are shown.

ponents of this complex (not shown in Fig. 12). Alternatively, the system can reach the conical state via stepwise bobber contraction. The presence of a second bobber influences this process: each contraction by one lattice constant corresponds to a metastable state, producing a sequence of shallow intermediate minima along the corresponding MEP [see the black line in Fig. 12(b)]. This contrasts with the case of a single bobber, where the energy profile exhibits shoulders instead [see the cyan line in Fig. 12(b)]. Eventually, the system relaxes into a configuration with two chiral bobbers whose sizes agree with the predictions of Ref. [37] (inset iv in Fig. 12). Afterward, one of the bobbers collapses, and the system reaches the same state as in the process involving the contraction of a single elongated bobber. From here, the system can either proceed directly to the conical phase via the escape of the bobber's Bloch point through the surface, or follow a higher-energy pathway in which a second Bloch point nucleates at the surface, forming an isolated globule state (see inset vi in Fig. 12) that reorients and then collapses through mutual annihilation of its Bloch points [see Fig. 12(c)].

Previous studies have reported chiral globules as stabilized through confinement or interaction with defects [38]. Recent work [74] suggests that globule states can also exist as true 3D solitons in certain parameter regimes without magnetostatics. Our results provide an alternative mechanism for the localization and stabilization of globule states via magnetostatic interactions. Without these interactions, the isolated globule is no longer metastable for the chosen set of parameters (see Appendix E).

Despite the complexity of metastable states and transition mechanisms revealed in this study, the picture summarized in Fig. 12 is likely incomplete. A more systematic exploration based on recursively connecting metastable states via saddle-point searches is expected to uncover additional transitions. This approach requires a method for escaping the convex region associated with each metastable state. One possibility is to follow specific low-lying modes of the system, which can be efficiently computed using a finite-difference scheme within an extended Rayleigh quotient framework. Other escape strategies may also be employed. Developing an optimal escape procedure for 3D magnetic systems remains an important direction for future research.

For comparison, we repeated the GMMF calculations for a system with the same interaction parameters but without magnetostatics, identical to the one studied by Rybakov *et al.* [37]. The results, which exhibit fewer metastable states overall, are summarized in Appendix E. As expected, including magnetostatic interactions increases the computational cost. However, the implemented GMMF method does not introduce additional scaling overhead beyond the computational complexity determined by the interactions present in the system (see Appendix F), making it well suited for large-scale simulations.

V. CONCLUSIONS AND DISCUSSION

In the GMMF/RQM method, convergence to SPs is achieved by maximizing the energy along one of the two lowest modes, defined by the eigenvectors corresponding to the two lowest eigenvalues of the Hessian, and minimizing it along all other directions. Instead of the computationally demanding task of repeatedly evaluating the Hessian and solving the eigenvalue problem, we introduce an efficient methodology based on the direct minimization of the generalized Rayleigh quotient using only the energy gradients. This becomes particularly important for large systems and/or systems with dense Hessians.

An important aspect of our methodology is the correct treatment of the geometry of the manifolds on which the optimization of the magnetic structure and minimization of the Rayleigh quotient are performed. In particular, optimization algorithms used in our method take into account the curvature of the corresponding manifolds via retraction and parallel transport. The GMMF/RQM method exhibits a high degree of computational efficiency and stability which we demonstrate in applications to 2D and 3D magnetic systems.

We show consistency with previously published results by identifying the three SPs corresponding to the mechanisms

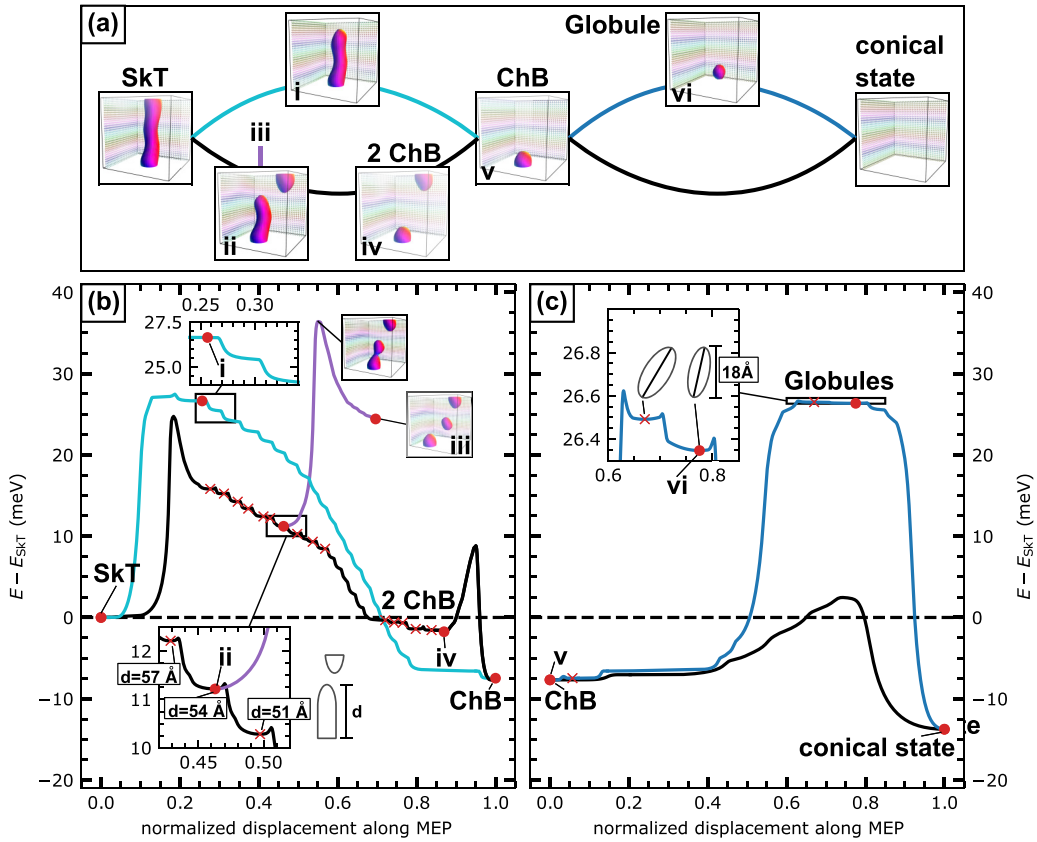

FIG. 12. (a) Graph showing metastable configurations (insets) and possible transitions between them in the 3D system with magnetostatic interactions, as obtained with the GMMF method. The magnetic configurations are visualized by the isosurfaces of $s_z = 0$ where the color code is described in Fig. 5(a). (b) Energy variation along the calculated MEPs: from the skyrmion tube (SkT) state to the chiral bobber (ChB) state via the elongated bobber (cyan line) and two ChB (black line) states, and from the state corresponding to two bobbers of different lengths to the metastable state involving a globule between two chiral bobbers (magenta line). The insets show zoomed-in views of the plots, magnetic configurations at specific points along the MEPs, and a sketch of the two-bobber state. (c) Energy variation along calculated MEPs connecting the ChB state to the conical state directly (black line) and via the isolated globule state (blue line). The insets show a zoomed-in view of the plot and sketches of the globule states. The red crosses mark position of the energy minima. The energy minima corresponding to metastable configurations shown in (a) are indicated with red dots. For each transition, the displacement along the MEP is normalized separately to align the positions of energy minima corresponding to the same magnetic configurations. The dashed line shows the zero-energy level corresponding to the relaxed skyrmion tube configuration.

of skyrmion transformation reported by Müller *et al.* [44]. In addition, we identify the fourth mechanism corresponding to the transformation of the skyrmion into a skyrmion bag.

An efficient computational scheme requiring only the evaluation of the gradient of the energy to compute the action of the Hessian has enabled the application of the GMMF method to a 3D system with magnetostatic interactions, and the discovery of a complex network of transitions between metastable chiral bobbers, skyrmion tubes, and globules. We obtain a mechanism for the collapse of a skyrmion tube via rupture followed by formation of metastable chiral bobbers, analogous to what has been reported by Rybakov *et al.* [37]. In addition, we identify a mechanism corresponding to detachment of the end of a skyrmion tube from the surface [75] and the formation of a new chiral bobber state where the equilibrium distance between the base and the terminating Bloch point is extended. Moreover, we report metastable magnetic globules appearing as isolated states due to magnetostatic interactions. It is important to realize that these results are obtained via straightforward application of the GMMF/RQM method without relying on subjective assumptions about the system.

While the GMMF/RQM method can be used independently to study transitions in various magnetic systems, it shows great promise when combined with other techniques such as the GNEB method or the CI-GNEB method where a climbing image is included to better converge on the SP [7]. Instead of converging all images representing the path to a low tolerance, the calculation can be terminated at an earlier stage and the highest-energy image used as a starting point for an efficient GMMF/RQM convergence on the SP. This is found to be the optimal strategy for magnetic systems, analogous to what has been found for atomic rearrangements [76].

The GMMF/RQM method can be integrated into a global optimization framework for magnetic textures by recursively traversing between local energy minima through first-order SPs [10]. Within this framework, calculating transition rates on the fly, using, for example, harmonic transition state theory, would enable the simulation of long timescale dynamics through the adaptive kinetic Monte Carlo algorithm [8,9].

To summarize, the GMMF/RQM method represents a valuable tool for studying transitions in various magnetic systems. This becomes particularly important in the context of topological magnetism where various 2D and 3D states have recently been discovered.

While the focus of this work is on locating first-order SPs, which are directly associated with transition mechanisms and energy barriers within HTST [1,2,23] and Kramers-Langer theory [3,4,77], the method can, in principle, be extended to identify higher-order SPs: stationary points characterized by more than one unstable mode. This would require inverting the magnetic force components along several modes simultaneously, using a generalized Rayleigh quotient to compute multiple eigenpairs of the Hessian. A second-order saddle point, for example, represents a maximum in energy along an energy ridge, and can be used to assess the accuracy of the harmonic approximation to TST. A generalization of our method to higher-order saddle points can be useful for other applications and remains a possible direction for future work.

The first phase of the SP search, the escape from the convex region, remains a challenging task. In our study of skyrmion collapse mechanisms in the 2D system, following various Hessian eigenvectors during the escape stage provided a straightforward means of introducing deformations that reflect the shape of the SP configurations. Thanks to the sparsity of the Hessian and the moderate system size, it was feasible, though not optimal, to construct the Hessian explicitly and compute the eigenvectors using standard techniques. A natural improvement is to obtain the relevant eigenvectors without constructing the full Hessian, for instance, via finite-difference evaluation of its action within an extended Rayleigh quotient framework. Further optimization is possible given that the precise determination of the escape direction is not critical: even crude approximations to the eigenvectors may suffice, or it may be possible to escape the convex region without explicitly following them at all. These considerations suggest substantial room for improving the escape stage. One promising direction is to exploit the symmetries of magnetic textures. Optimization of the escape stage remains a subject of future research.

ACKNOWLEDGMENTS

M.S. is grateful to A. Goswami and G. P. Müller for fruitful discussions. H.S. is grateful to M. Görzen and S. Heinze for fruitful discussions. This work received financial support from the Icelandic Research Fund (Grants No. 239435 and No. 217750), the University of Iceland Research Fund (Grants No. 15673 and No. 15661), the Swedish Research Council (Grant No. 2020-05110), and the Crafoord Foundation (Grant No. 20231063). The calculations were carried out at the high-performance computing resources available at the Kiel University Computing Centre and at the Icelandic Research e-Infrastructure facility supported by the Icelandic Infrastructure Fund.

DATA AVAILABILITY

The data that support the findings of this article are not publicly available upon publication because it is not technically feasible and/or the cost of preparing, depositing, and hosting the data would be prohibitive within the terms of this research project. The data are available from the authors upon reasonable request.

APPENDIX A: SYSTEM OF FOUR MAGNETIC MOMENTS ILLUSTRATING MODE CROSSING

To illustrate the mode crossings in Fig. 3, a system of four magnetic moments placed in the corners of a square is considered. Only the nearest-neighbor moments are coupled via the exchange J and a magnetic field in the negative z direction is applied. Furthermore, the uniaxial anisotropy favors alignment along the $\pm z$ direction. The Hamiltonian of the system reads as

$$\tilde{E} = -J(\vec{s}_1 \cdot \vec{s}_2 + \vec{s}_1 \cdot \vec{s}_3 + \vec{s}_2 \cdot \vec{s}_4 + \vec{s}_3 \cdot \vec{s}_4) - \mu \sum_{i=1}^{4} \vec{B} \cdot \vec{s}_i - \sum_{i=1}^{4} K(\vec{s}_i \cdot \vec{e}_z)^2 \tag{A1}$$

with $J = 0.5$ eV, K $= 1.0$ eV, and $\vec{B}_{\text{ext}} = -1.0\hat{e}_z$ T as well as $\mu = 1\,\mu_B$. For these parameters, the parallel alignment of the magnetic moments in the $+z$ direction is a local energy minimum configuration. From this minimum configuration, a suitable start configuration for the application of the GMMF method is obtained by rotating two magnetic moments sitting on opposite corners of the square. The lowest eigenvalue spectrum of the system during this rotation is visualized in Fig. 3(a).

APPENDIX B: PSEUDOCODE FOR OPTIMIZATION OF THE RAYLEIGH QUOTIENT

The optimization is represented by the four algorithms. The main routine is given in Algorithm 1. To compute the search direction, we use the well-known "two loop recursion," listed in Algorithm 2. Algorithm 1, in combination with Algorithm 2, constitutes a fairly standard L-BFGS method with some exceptions: A minor one is that the algorithm is being applied to matrices instead of, as perhaps more commonly seen, vectors. The other, much more important, is the use of the `Parallel transport` and `Retraction` functions to move across the Grassmann manifold, in a way that respects its inherent geometry. These two are implemented in Algorithms 3 and 4, respectively, and make use of equations given by Edelmann *et al.* [50].

APPENDIX C: EVALUATION OF THE HESSIAN MATRIX

The Hessian matrix for a magnetic system characterized by N constraints on the length of the magnetic moments can be computed as follows. First, the $3N \times 3N$ matrix H^{3N} of the second-order derivatives of the energy with respect to the Cartesian components of the magnetic moments is calculated. After that, the shape operator $\mathcal{L}$ is subtracted from H^{3N}. The shape operator is a diagonal matrix of the form

$$\mathcal{L} = \begin{pmatrix} L_1 & \dots & 0 \\ \vdots & \ddots & \vdots \\ 0 & \dots & L_N \end{pmatrix}, \tag{C1}$$

ALGORITHM 1. L-BFGS optimizer for the generalized Rayleigh quotient.

Require: Initial point X on the Grassmann manifold $G_{2,2N}$, Hessian matrix H, tolerance ϵ, maximum memory m
Ensure: Solution X that spans the minimal invariant subspace of H
Initialize $k \leftarrow 0$
Initialize $X_0 \leftarrow X$
Initialize the history $S \leftarrow [], Y \leftarrow [], \rho \leftarrow []$
while $k <$ maxIterations **do**
// Here, we denote the action of the Hessian as HX
// In practice, we use the finite-difference scheme
// described in Sec. II B
$G_k \leftarrow 2X_k[HX_k - X_k(X_k^T HX_k)]$
if $\|G_k\|_F < \epsilon$ **then**
break
end if
// Transport the history to the current tangent frame
if len$(S) > 0$ **then**
$S_i \leftarrow \texttt{Transport}(X_{k-1}, S_i, P, \Sigma, V) \quad \forall\, S_i \in S$
$Y_i \leftarrow \texttt{Transport}(X_{k-1}, Y_i, P, \Sigma, V) \quad \forall\, Y_i \in Y$
end if
if k > 1 **then**
// Append to the history
Append Λ to S
Append $G_k - \texttt{Transport}(X_{k-1}, G_{k-1}, P, \Sigma, V)$ to Y
Append $\mathrm{tr}[(X_k - X_{k-1})^T (G_k - G_{k-1})]^{-1}$ to ρ
if len$(S) > m$ **then**
Delete oldest entry of S, Y, and ρ
end if
// Curvature rejection condition
if $\rho_{-1} < 0$ **then**
// Reset the history
$S \leftarrow [], Y \leftarrow [], \rho \leftarrow []$
end if
end if
// Compute the search direction via two-loop recursion
$\Lambda \leftarrow \texttt{TwoLoopRecursion}(S, Y, \rho, G_k)$
// Perform compact singular value
// decomposition of Λ such that $\Lambda = P\Sigma V^T$
$P, \Sigma, V \leftarrow \texttt{SVD}(\Lambda)$
// Update X via retraction
$X_{k+1} \leftarrow \texttt{Retraction}(X_k, P, \Sigma, V)$
$k \leftarrow k + 1$
end while

with

$$L_i = \begin{pmatrix} \vec{s}_i \cdot \vec{\nabla}_i E & 0 & 0 \\ 0 & \vec{s}_i \cdot \vec{\nabla}_i E & 0 \\ 0 & 0 & \vec{s}_i \cdot \vec{\nabla}_i E \end{pmatrix}. \tag{C2}$$

Finally, the matrix $U \in \mathbb{R}^{3N \times 2N}$ is applied, that projects the embedding space vectors into the tangent space of the current configuration $\boldsymbol{s}$ (see Refs. [44,51]):

$$H = U^T (H^{3N} - \mathcal{L}) U. \tag{C3}$$

ALGORITHM 2. Two-loop recursion.

function TwoLoopRecursion(S, Y, ρ, G)
$\Lambda \leftarrow G$
$s \leftarrow$ len(S)
for $i = s$ down to 1 **do**
$\alpha_i \leftarrow \rho_i \mathrm{tr}(S_i^T \Lambda)$
$\Lambda \leftarrow \Lambda - \alpha_i Y_i$
end for
if $s > 0$ **then**
// Initial diagonal approximation
// for the inverse Hessian
$H^{s-1} \leftarrow \rho_i^{-1} \sqrt{\mathrm{tr}({Y_{s-1}}^T Y_{s-1})}$
$\Lambda \leftarrow H^{s-1} \Lambda$
end if
for $i = 1$ to s **do**
$\beta \leftarrow \rho_i \mathrm{tr}(Y_i^T \Lambda)$
$\Lambda \leftarrow \Lambda + (\alpha_i - \beta) S_i$
end for
// Minus sign for minimization
return $-\Lambda$
end function

APPENDIX D: NUMERICAL PARAMETERS FOR GMMF CALCULATIONS

The GMMF calculations are considered converged if the maximum norm of the effective field components drops below a value of 10^{-12} eV:

$$\max_{i \in \{1,\ldots,N\}} |\vec{b}_i| < 10^{-12}\ \text{eV}. \tag{D1}$$

The L-BFGS based GMMF algorithm is used without a line search procedure. As described in Ref. [56] we restrict the maximum step length with a parameter $\vartheta_{\max}$. The number of memory quantities taken into account is $m = 3$ for all calculations in this publication. For the GMMF calculations presented in Sec. IV A we always chose $\vartheta_{\max}^{\mathrm{GMMF}} = 0.5$. Also the L-BFGS solver of the RQM method was set to $\vartheta_{\max}^{\mathrm{RQM}} = 0.5$. The calculation of the two lowest modes within the RQM method is considered converged if the Frobenius norm of the Rayleigh gradient drops below 10^{-8} eV.

APPENDIX E: EFFECT OF EXCLUDING MAGNETOSTATICS ON THE COLLAPSE MECHANISMS OF 3D MAGNETIC STATES

Following the approach described in Sec. IV A, we compute the SPs, energy minima, and MEPs for the system

ALGORITHM 3. Parallel transport.

function Transport(X, A, P, Σ, V)
// The parentheses are necessary to ensure a
// computationally efficient order of evaluation
$T_1 A \leftarrow -XV\ \sin(\Sigma)(P^T A)$
$T_2 A \leftarrow P\ \cos(\Sigma)(P^T A)$
$T_3 A \leftarrow A - P(P^T A)$
return $T_1 A + T_2 A + T_3 A$
end function

ALGORITHM 4. Retraction.

function `Retraction`(X, P, Σ, V)
  $X' \leftarrow XV\ \cos(\Sigma)V^T + P\ \sin(\Sigma)V^T$
  // Prevent accumulation of numerical errors
  Orthonormalize columns of X' with QR algorithm
  return X'
end function

without magnetostatic interactions. Additionally, we test whether SPs identified in the system with magnetostatics persist by using the corresponding configurations as starting points for GMMF optimization in the system without magnetostatics. The results of these calculations are summarized in Fig. 13.

Overall, excluding magnetostatics results in fewer metastable states and possible transitions. Nevertheless, rupture of the skyrmion tube and detachment of its end from the surface are still present. In the absence of magnetostatics, however, these two mechanisms of the skyrmion tube collapse exhibit nearly equal energy barriers. Consistent with Ref. [37], the rupture of the tube results directly in the formation of two short chiral bobbers. No intermediate states appear along this transition, which is in contrast to the case with magnetostatic interactions. Interestingly, the metastable elongated bobber still forms following detachment of the end of the tube from the surface.

As in the case with magnetostatics, both collapse mechanisms eventually lead to a single bobber state. From there, the system proceeds directly to the conical phase via the escape of the bobber's Bloch point through the surface. No alternative collapse mechanism for the bobber was found. In particular, no pathway involving the formation of globules was obtained. Moreover, globules do not form metastable isolated

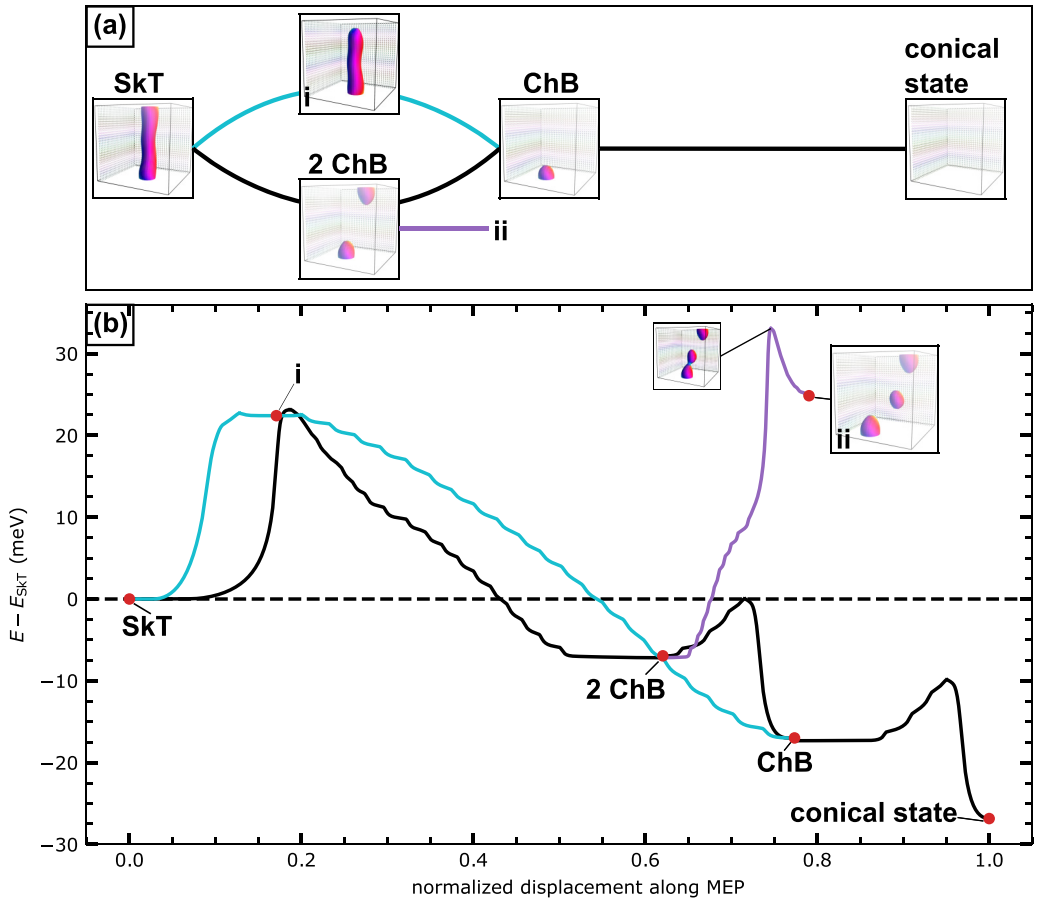

FIG. 13. (a) Graph showing metastable configurations (insets) and possible transitions between them in the 3D system without magnetostatic interactions, as obtained with the GMMF method. The magnetic configurations are visualized by the isosurfaces of $s_z = 0$ where the color code is described in Fig. 5(a). (b) Energy variation along the calculated MEPs: from the skyrmion tube (SkT) state to the conical state via the two-bobber state (black line), from the SkT state to the chiral bobber (ChB) state via the elongated bobber state (cyan line), and from the two ChB state to the state involving a globule between two chiral bobbers (magenta line). The insets show magnetic configurations at specific points along the MEPs. The red dots mark position of the energy minima. For each transition, the displacement along the MEP is normalized separately to align the positions of energy minima corresponding to the same magnetic configurations. The dashed line shows the zero-energy level corresponding to the relaxed skyrmion tube configuration.

configurations in the absence of magnetostatics for the chosen set of parameter values. However, they can still become metastable near defects [38]. In particular, the state involving a globule positioned between two bobbers is metastable even without magnetostatics and is connected to the two-bobber configuration.

APPENDIX F: SCALING OF THE COMPUTATIONAL EFFORT

To assess the computational performance of the GMMF method, we examine its scaling with the number of magnetic moments N in the system. A key computational step in the method is the evaluation of the gradient of the Rayleigh quotient, $\nabla R(X)$ [see Eq. (14)], which dominates the cost per iteration during saddle-point searches. We therefore use the mean CPU time required for a single gradient evaluation as a representative benchmark.

Figure 14 shows the CPU time as a function of N for cubic systems with and without magnetostatic interactions, where magnetic moments are oriented randomly. The observed scaling reflects the complexity determined by the underlying interactions: for systems without magnetostatics, the scaling is linear, $O(N)$. When magnetostatic interactions are included, the scaling follows $O(N \log N)$ due to the use of fast Fourier transform-based methods. While the distinction between linear and $O(N \log N)$ scaling is subtle in the current system size range, the data remain consistent with the expected behavior.

Crucially, the GMMF algorithm itself introduces no additional scaling overhead beyond what is required to compute the system energy and its gradient. This makes it well suited for application to large systems, including those with long-range interactions.

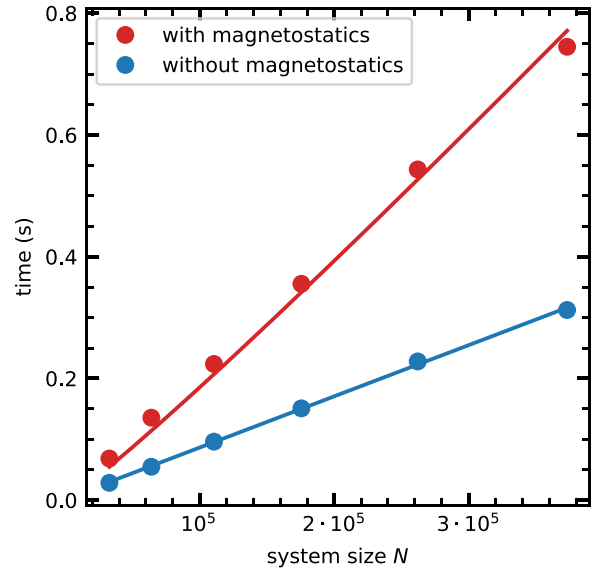

FIG. 14. Mean CPU time required for a single evaluation of the Rayleigh quotient gradient $\nabla R(X)$ [see Eq. (14)] as a function of the number of magnetic moments N in a cubic system with and without magnetostatic interactions, as indicated in the legend. The blue (red) line shows the linear ($N \log N$) fit.

[1] E. Wigner, The transition state method, Trans. Faraday Soc. **34**, 29 (1938).

[2] G. H. Vineyard, Frequency factors and isotope effects in solid state rate processes, J. Phys. Chem. Solids **3**, 121 (1957).

[3] H. A. Kramers, Brownian motion in a field of force and the diffusion model of chemical reactions, Physica (Amsterdam) **7**, 284 (1940).

[4] J. Langer, Statistical theory of the decay of metastable states, Ann. Phys. **54**, 258 (1969).

[5] D. V. Berkov, Magnetization dynamics including thermal fluctuations: Basic phenomenology, fast remagnetization processes and transitions over high-energy barriers, in *Handbook of Magnetism and Advanced Magnetic Materials* (Wiley, Hoboken, NJ, 2007), Vol. 2, pp. 795–823.

[6] H. Jónsson, G. Mills, and K. W. Jacobsen, Nudged elastic band method for finding minimum energy paths of transitions, in *Classical and Quantum Dynamics in Condensed Phase Simulations*, edited by B. J. Berne, G. Ciccotti, and D. F. Coker (World Scientific, Singapore, 1998), pp. 385–404.

[7] P. F. Bessarab, V. M. Uzdin, and H. Jónsson, Method for finding mechanism and activation energy of magnetic transitions, applied to skyrmion and antivortex annihilation, Comput. Phys. Commun. **196**, 335 (2015).

[8] G. Henkelman and H. Jónsson, Long time scale kinetic Monte Carlo simulations without lattice approximation and predefined event table, J. Chem. Phys. **115**, 9657 (2001).

[9] H. Jónsson, Simulation of surface processes, Proc. Natl. Acad. Sci. USA **108**, 944 (2011).

[10] M. Plasencia, A. Pedersen, A. Arnaldsson, J.-C. Berthet, and H. Jónsson, Geothermal model calibration using a global minimization algorithm based on finding saddle points and minima of the objective function, Comput. Geosci. **65**, 110 (2014).

[11] D. M. Einarsdóttir, A. Arnaldsson, F. Óskarsson, and H. Jónsson, Path optimization with application to tunneling, in *Applied Parallel and Scientific Computing*, edited by K. Jónasson (Springer, Berlin, 2012), pp. 45–55.

[12] V. Ásgeirsson, A. Arnaldsson, and H. Jónsson, Efficient evaluation of atom tunneling combined with electronic structure calculations, J. Chem. Phys. **148**, 102334 (2018).

[13] S. M. Vlasov, P. F. Bessarab, I. S. Lobanov, M. N. Potkina, V. M. Uzdin, and H. Jónsson, Magnetic skyrmion annihilation by quantum mechanical tunneling, New J. Phys. **22**, 083013 (2020).

[14] I. A. Nosikov, M. V. Klimenko, G. A. Zhbankov, A. V. Podlesnyi, V. A. Ivanova, and P. F. Bessarab, Generalized force approach to point-to-point ionospheric ray tracing and systematic identification of high and low rays, IEEE Trans. Antennas Propag. **68**, 455 (2020).

[15] B. Peters, *Reaction Rate Theory and Rare Events* (Elsevier, Amsterdam, 2017).

[16] G. Henkelman and H. Jónsson, A dimer method for finding saddle points on high dimensional potential surfaces using only first derivatives, J. Chem. Phys. **111**, 7010 (1999).
[17] R. Malek and N. Mousseau, Dynamics of Lennard-Jones clusters: A characterization of the activation-relaxation technique, Phys. Rev. E **62**, 7723 (2000).
[18] A. Pedersen, S. F. Hafstein, and H. Jónsson, Efficient sampling of saddle points with the minimum-mode following method, SIAM J. Sci. Comput. **33**, 633 (2011).
[19] M. P. Gutiérrez, C. Argáez, and H. Jónsson, Improved minimum mode following method for finding first order saddle points, J. Chem. Theory Comput. **13**, 125 (2017).
[20] C. Lanczos, An iteration method for the solution of the eigenvalue problem of linear differential and integral operators, J. Res. Natl. Bureau Stand. **45**, 255 (1950).
[21] E. R. Davidson, The iterative calculation of a few of the lowest eigenvalues and corresponding eigenvectors of large real-symmetric matrices, J. Comput. Phys. **17**, 87 (1975).
[22] W. T. Coffey, D. A. Garanin, and D. J. Mccarthy, Crossover formulas in the kramers theory of thermally activated escape rates–application to spin systems, in *Advances in Chemical Physics* (Wiley, Hoboken, NJ, 2001), pp. 483–765.
[23] P. F. Bessarab, V. M. Uzdin, and H. Jónsson, Harmonic transition-state theory of thermal spin transitions, Phys. Rev. B **85**, 184409 (2012).
[24] P. F. Bessarab, V. M. Uzdin, and H. Jónsson, Potential energy surfaces and rates of spin transitions, Z. Phys. Chem. **227**, 1543 (2013).
[25] I. S. Lobanov, H. Jónsson, and V. M. Uzdin, Mechanism and activation energy of magnetic skyrmion annihilation obtained from minimum energy path calculations, Phys. Rev. B **94**, 174418 (2016).
[26] D. Cortés-Ortuño, W. Wang, M. Beg, R. A. Pepper, M.-A. Bisotti, R. Carey, M. Vousden, T. Kluyver, O. Hovorka, and H. Fangohr, Thermal stability and topological protection of skyrmions in nanotracks, Sci. Rep. **7**, 4060 (2017).
[27] S. von Malottki, B. Dupé, P. F. Bessarab, A. Delin, and S. Heinze, Enhanced skyrmion stability due to exchange frustration, Sci. Rep. **7**, 12299 (2017).
[28] P. F. Bessarab, G. P. Müller, I. S. Lobanov, F. N. Rybakov, N. S. Kiselev, H. Jónsson, V. M. Uzdin, S. Blügel, L. Bergqvist, and A. Delin, Lifetime of racetrack skyrmions, Sci. Rep. **8**, 3433 (2018).
[29] B. Heil, A. Rosch, and J. Masell, Universality of annihilation barriers of large magnetic skyrmions in chiral and frustrated magnets, Phys. Rev. B **100**, 134424 (2019).
[30] D. Cortés-Ortuño, N. Romming, M. Beg, K. von Bergmann, A. Kubetzka, O. Hovorka, H. Fangohr, and R. Wiesendanger, Nanoscale magnetic skyrmions and target states in confined geometries, Phys. Rev. B **99**, 214408 (2019).
[31] H. Schrautzer, S. von Malottki, P. F. Bessarab, and S. Heinze, Effects of interlayer exchange on collapse mechanisms and stability of magnetic skyrmions, Phys. Rev. B **105**, 014414 (2022).
[32] M. A. Goerzen, S. von Malottki, S. Meyer, P. F. Bessarab, and S. Heinze, Lifetime of coexisting sub-10 nm zero-field skyrmions and antiskyrmions, npj Quantum Mater. **8**, 54 (2023).
[33] J. Hagemeister, A. Siemens, L. Rózsa, E. Y. Vedmedenko, and R. Wiesendanger, Controlled creation and stability of $k\pi$ skyrmions on a discrete lattice, Phys. Rev. B **97**, 174436 (2018).
[34] L. Desplat, J.-V. Kim, and R. L. Stamps, Paths to annihilation of first- and second-order (anti)skyrmions via (anti)meron nucleation on the frustrated square lattice, Phys. Rev. B **99**, 174409 (2019).
[35] V. M. Kuchkin, B. Barton-Singer, F. N. Rybakov, S. Blügel, B. J. Schroers, and N. S. Kiselev, Magnetic skyrmions, chiral kinks, and holomorphic functions, Phys. Rev. B **102**, 144422 (2020).
[36] V. M. Kuchkin, N. S. Kiselev, F. N. Rybakov, and P. F. Bessarab, Tailed skyrmions—An obscure branch of magnetic solitons, Front. Phys. **11**, 1171079 (2023).
[37] F. N. Rybakov, A. B. Borisov, S. Blügel, and N. S. Kiselev, New type of stable particlelike states in chiral magnets, Phys. Rev. Lett. **115**, 117201 (2015).
[38] G. P. Müller, F. N. Rybakov, H. Jónsson, S. Blügel, and N. S. Kiselev, Coupled quasimonopoles in chiral magnets, Phys. Rev. B **101**, 184405 (2020).
[39] V. M. Kuchkin and N. S. Kiselev, Homotopy transitions and 3D magnetic solitons, APL Mater. **10**, 071102 (2022).
[40] I. S. Lobanov and V. M. Uzdin, Lifetime, collapse, and escape paths for hopfions in bulk magnets with competing exchange interactions, Phys. Rev. B **107**, 104405 (2023).
[41] M. Sallermann, H. Jónsson, and S. Blügel, Stability of hopfions in bulk magnets with competing exchange interactions, Phys. Rev. B **107**, 104404 (2023).
[42] Y. Li, Y. Zang, R. Chen, and C. Moutafis, Tailoring energy barriers of bloch-point-mediated transitions between topological spin textures, Phys. Rev. B **109**, 024418 (2024).
[43] Y. L. A. Schmerwitz, G. Levi, and H. Jónsson, Calculations of excited electronic states by converging on saddle points using generalized mode following, J. Chem. Theory Comput. **19**, 3634 (2023).
[44] G. P. Müller, P. F. Bessarab, S. M. Vlasov, F. Lux, N. S. Kiselev, S. Blügel, V. M. Uzdin, and H. Jónsson, Duplication, collapse, and escape of magnetic skyrmions revealed using a systematic saddle point search method, Phys. Rev. Lett. **121**, 197202 (2018).
[45] P. F. Bessarab, V. M. Uzdin, and H. Jónsson, Calculations of magnetic states and minimum energy paths of transitions using a noncollinear extension of the alexander-anderson model and a magnetic force theorem, Phys. Rev. B **89**, 214424 (2014).
[46] A. V. Ivanov, D. Dagbartsson, J. Tranchida, V. M. Uzdin, and H. Jónsson, Efficient optimization method for finding minimum energy paths of magnetic transitions, J. Phys.: Condens. Matter **32**, 345901 (2020).
[47] H. Bocquet and P. M. Derlet, Searching for activated transitions in complex magnetic systems, Phys. Rev. B **108**, 174419 (2023).
[48] Intel math kernel library (2024.2.2) (2024).
[49] V. P. Antropov, M. I. Katsnelson, B. N. Harmon, M. van Schilfgaarde, and D. Kusnezov, Spin dynamics in magnets: Equation of motion and finite temperature effects, Phys. Rev. B **54**, 1019 (1996).
[50] A. Edelman, T. A. Arias, and S. T. Smith, The geometry of algorithms with orthogonality constraints, SIAM J. Matrix Anal. Appl. **20**, 303 (1998).
[51] A. S. Varentcova, S. von Malottki, M. N. Potkina, G. Kwiatkowski, S. Heinze, and P. F. Bessarab, Toward room-temperature nanoscale skyrmions in ultrathin films, npj Comput. Mater. **6**, 193 (2020).

[52] K. Ohno and S. Maeda, A scaled hypersphere search method for the topography of reaction pathways on the potential energy surface, Chem. Phys. Lett. **384**, 277 (2004).

[53] S. Maeda, Y. Watanabe, and K. Ohno, A scaled hypersphere interpolation technique for efficient construction of multidimensional potential energy surfaces, Chem. Phys. Lett. **414**, 265 (2005).

[54] P.-A. Absil, R. Mahony, and R. Sepulchre, *Optimization Algorithms on Matrix Manifolds* (Princeton University Press, Princeton, NJ, 2008).

[55] D. C. Liu and J. Nocedal, On the limited memory BFGS method for large scale optimization, Math. Program. **45**, 503 (1989).

[56] A. V. Ivanov, V. M. Uzdin, and H. Jónsson, Fast and robust algorithm for energy minimization of spin systems applied in an analysis of high temperature spin configurations in terms of skyrmion density, Comput. Phys. Commun. **260**, 107749 (2021).

[57] G. L. G. Sleijpen and H. A. Van der Vorst, A Jacobi–Davidson iteration method for linear eigenvalue problems, SIAM Rev. **42**, 267 (2000).

[58] G. W. Stewart, A Krylov–Schur algorithm for large eigenproblems, SIAM J. Matrix Anal. Appl. **23**, 601 (2002).

[59] C. Brezinski, Some pioneers of extrapolation methods, in *The Birth of Numerical Analysis* (World Scientific, Singapoire, 2010), pp. 1–22.

[60] L. F. Richardson, IX. The approximate arithmetical solution by finite differences of physical problems involving differential equations, with an application to the stresses in a masonry dam, Philos. Trans. R. Soc. London, Ser. A **210**, 307 (1911).

[61] L. F. Richardson and J. A. Gaunt, VIII. The deferred approach to the limit, Philos. Trans. R. Soc. London, Ser. A **226**, 299 (1927).

[62] A. Pedersen, J.-C. Berthet, and H. Jónsson, Simulated annealing with coarse graining and distributed computing, in *Applied Parallel and Scientific Computing*, edited by K. Jónasson (Springer, Berlin, 2012), pp. 34–44.

[63] S. T. Chill, M. Welborn, R. Terrell, L. Zhang, J.-C. Berthet, A. Pedersen, H. Jónsson, and G. Henkelman, Eon: Software for long time simulations of atomic scale systems, Modell. Simul. Mater. Sci. Eng. **22**, 055002 (2014).

[64] O. Eriksson, A. Bergman, L. Bergqvist, and J. Hellsvik, *Atomistic Spin Dynamics: Foundations and Applications* (Oxford University Press, Oxford, 2017).

[65] Q. Xu, I. P. Miranda, M. Pereiro, F. N. Rybakov, D. Thonig, E. Sjöqvist, P. F. Bessarab, A. Bergman, O. Eriksson, P. Herman, and A. Delin, Metaheuristic conditional neural network for harvesting skyrmionic metastable states, Phys. Rev. Res. **5**, 043199 (2023).

[66] F. Zheng, F. N. Rybakov, A. B. Borisov, D. Song, S. Wang, Z.-A. Li, H. Du, N. S. Kiselev, J. Caron, A. Kovács, M. Tian, Y. Zhang, S. Blügel, and R. E. Dunin-Borkowski, Experimental observation of chiral magnetic bobbers in b20-type fege, Nat. Nanotechnol. **13**, 451 (2018).

[67] J. W. Cooley and J. W. Tukey, An algorithm for the machine calculation of complex fourier series, Math. Comput. **19**, 297 (1965).

[68] N. Hayashi, K. Saito, and Y. Nakatani, Calculation of demagnetizing field distribution based on fast fourier transform of convolution, Jpn. J. Appl. Phys. **35**, 6065 (1996).

[69] H. J. G. Draaisma and W. J. M. de Jonge, Surface and volume anisotropy from dipole-dipole interactions in ultrathin ferromagnetic films, J. Appl. Phys. **64**, 3610 (1988).

[70] V. L. Zhang, C. G. Hou, K. Di, H. S. Lim, S. C. Ng, S. D. Pollard, H. Yang, and M. H. Kuok, Eigenmodes of néel skyrmions in ultrathin magnetic films, AIP Adv. **7**, 055212 (2017).

[71] L. Desplat, D. Suess, J.-V. Kim, and R. L. Stamps, Thermal stability of metastable magnetic skyrmions: Entropic narrowing and significance of internal eigenmodes, Phys. Rev. B **98**, 134407 (2018).

[72] S. von Malottki, P. F. Bessarab, S. Haldar, A. Delin, and S. Heinze, Skyrmion lifetime in ultrathin films, Phys. Rev. B **99**, 060409(R) (2019).

[73] See Supplemental Material at http://link.aps.org/supplemental/10.1103/z673-hhnp for details of the calculations illustrating the breakdown of the skyrmion escape mechanism.

[74] V. M. Kuchkin, N. S. Kiselev, A. Haller, I. C. V. Liščák, A. Michels, and T. L. Schmidt, Stability and nucleation of dipole strings in uniaxial chiral magnets, Phys. Rev. B **111**, 174410 (2025).

[75] G. P. Müller, M. Hoffmann, C. Dißelkamp, D. Schürhoff, S. Mavros, M. Sallermann, N. S. Kiselev, H. Jónsson, and S. Blügel, Spirit: Multifunctional framework for atomistic spin simulations, Phys. Rev. B **99**, 224414 (2019).

[76] V. Ásgeirsson, B. O. Birgisson, R. Bjornsson, U. Becker, F. Neese, C. Riplinger, and H. Jónsson, Nudged elastic band method for molecular reactions using energy-weighted springs combined with eigenvector following, J. Chem. Theory Comput. **17**, 4929 (2021).

[77] G. Fiedler, J. Fidler, J. Lee, T. Schrefl, R. L. Stamps, H. B. Braun, and D. Suess, Direct calculation of the attempt frequency of magnetic structures using the finite element method, J. Appl. Phys. **111**, 093917 (2012).